Influence of Coupled Radiation and Ablation on the Aerothermodynamic Environment of Planetary Entry Vehicles

Christopher O. Johnston, Peter A. Gnoffo, and Alireza Mazaheri
NASA Langley Research Center
Hampton, VA 23681-2199
USA

Christopher.O.Johnston@nasa.gov

ABSTRACT

A review of recently published coupled radiation and ablation capabilities involving the simulation of hypersonic flowfields relevant to Earth, Mars, or Venus entry is presented. The three fundamental mechanisms of radiation coupling are identified as radiative cooling, precursor photochemistry, and ablation-radiation interaction. The impact of these mechanisms are shown to be significant for a 3 m radius sphere entering Earth at hypothetical Mars return conditions (∼15 km/s). To estimate the influence precursor absorption on the radiative flux for a wide range of conditions, a simplified approach is developed that requires only the non-precursor solution. Details of a developed coupled ablation approach, which is capable of treating both massively ablating flowfields in the sublimation regime and weakly ablating diffusion–limited oxidation cases, are presented. A review of the two primary uncoupled ablation approximations, identified as the blowing correction and film coefficient approximations, is made and their impact for Earth and Mars entries is shown to be significant for recession and convective heating predictions. Fully coupled ablation and radiation simulations are presented for the Mars return sphere throughout its entire trajectory. Applying to the Mars return sphere the Pioneer-Venus heritage carbon phenolic heatshield, which has properties available in the open literature, the differences between steady state ablation and coupling to a material response code are shown to be significant.

1.0 INTRODUCTION

NASA's goal of manned exploration beyond low Earth orbit presents new challenges to the simulation of the aerothermodynamic environment resulting from such missions. For example, a return to Earth from Mars or an asteroid may require Earth entry velocities as high as 16 km/s, which would result in massive ablation and significant radiative heating. The influence of ablation-product injection into the flowfield (coupled ablation) and radiative energy exchange on the flowfield (coupled radiation) are required for the accurate prediction of radiative and convective heat rates, or more importantly, the material response of the heat shield. An illustration of these coupled phenomena is presented in Fig. 1, where the components shown in ovals represent mechanisms through which coupled ablation and radiation influence the flowfield. Modeling the influence of these mechanisms on the components of the surface energy balance, listed in the white boxes, represents the primary goal of an aerothermodynamic simulation. As will be shown in this paper, uncoupled techniques for approximately treating these coupled ablation and radiation phenomena, based on non-radiating and non-ablating flowfield

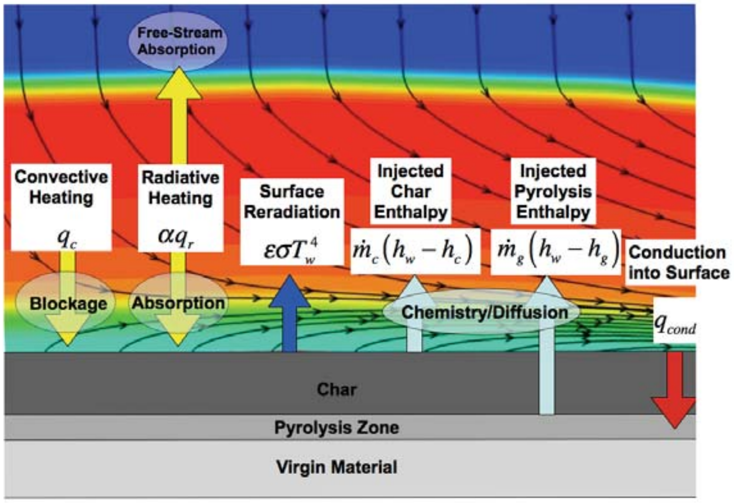

Figure 1: Energy balance for a charring ablator.

solutions, are found to introduce significant errors for many cases. In regards to efficient heat shield design, the significance of these errors are magnified by the fact that, as the influence of coupled ablation and radiation increases, the mass of the ablator becomes a larger fraction of the total entry system mass. This is illustrated in Fig. 2, which presents the reduction due to ablation in the total (radiative and convective) heating at the stagnation point of various NASA missions (including a hypothetical Mars return case, which will be discussed later) as a function of the mass fraction of the thermal protection system (TPS). It is seen that as the influence of ablation on the heating increases, indicating the increased importance of a coupled ablation analysis, the TPS mass fraction increases, indicating the increased importance of minimizing the ablator thickness for efficient vehicle design. Similarly, the influence of coupled radiation is found to increase as a function of TPS mass fraction. With NASA's previously mentioned goal of manned exploration beyond low Earth orbit, these observations provide significant motivation for the development of the coupled ablation and radiation simulation capability.

The goal of this paper is to present an overview of recent advancements to NASA's coupled radiation and ablation capability. The subject of coupled radiation is discussed in Section 2, which reviews the flowfield and radiation models applied throughout this work, followed by discussions of the three fundamental mechanisms of coupled radiation: 1) "radiative cooling", 2) ablation-radiation interaction, and 3) precursor photochemistry. The subject of coupled ablation is discussed in Section 3, which provides details of the developed coupled ablation procedure and investigates the influence of uncoupled ablation approximations for Earth and Mars entry cases. Finally, Section 4 applies the coupled radiation and ablation capability to a complete Mars return to Earth trajectory. Surface recession and in-depth material response are presented to show the potential of using Pioneer-Venus heritage carbon phenolic for such a mission.

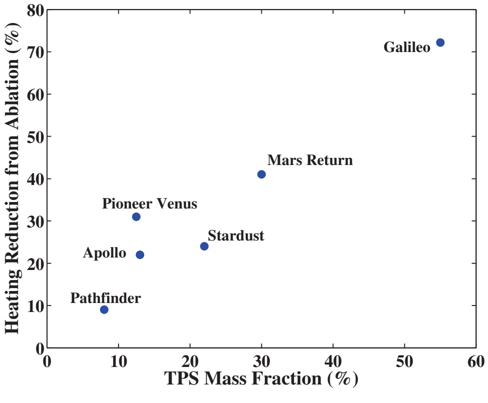

Figure 2: Specified ablation rates and wall temperature.

2.0 COUPLED RADIATION

Shock layer radiation influences a reentry flowfield through three fundamental physical mechanisms: 1) "radiative cooling", 2) ablation-radiation interaction, and 3) precursor photochemistry. To simulate these phenomena, a thermochemical nonequilibrium flowfield coupled to a detailed radiation and ablation model is required. While details regarding coupled ablation are deferred until later in this paper, the nonequilibrium flowfield and radiation model are presented in the next two subsections, followed by discussions and examples of the three coupled radiation influences mentioned above.

2.1 Flowfield Modeling

The LAURA v5 Navier-Stokes solver[1] was applied in this work, which includes a two-temperature thermochemcial nonequilibrium model and the following 26 species throughout the flowfield (including the wall): N, N^+, NO, NO^+, N_2, $N_2{}^+$, O, O^+, O_2, $O_2{}^+$, e^-, C, C^+, CO, CO_2, C_2, C_3, C_4, C_5, C_2H, C_2H_2, CN, H, H_2, HCN, and CH. The thermodynamic properties for these species were obtained from Gordon and Mcbride[2]. The transport properties were obtained from Wright et al.[3, 4] where available. The remaining species were treated using the approximate approach of Svehla[5] modified as suggested by Park[6]. The chemical reaction rates applied were the same as those applied by Johnston et al. [7]. The baseline predictions are assumed completely turbulent using the Cebeci-Smith turbulence model[8, 9] with a turbulent Schmidt number of 0.9.

2.2 Radiation Modeling

All radiation computations in this work are made using the state-of-the-art HARA radiation code. This code was created with the intention of applying it to coupled radiation and ablation simulations. A features that makes HARA ideal for this application is its ability to treat molecular bands using either the efficient smeared rotational band (SRB) approach or the rigorous, but orders of magnitude more computationally expensive, line-by-line approach. Depending on the importance and anticipated optical thickness of an individual band system, the user may specify which band systems, if any, are treated using the LBL approach. Another feature that make HARA ideal for coupled analyses is its comprehensive set of radiation properties, including spectral data and non-Boltzmann models for diatomic molecules and atomic species.

Table 1: Oscillator strength uncertainties for molecular band systems resulting from ablation products.

Band System	+/- Uncertainty
CO Fourth-Positive [10, 11]	40%
CN Red[10, 11]	30%
CN Violet[10, 11]	15%
C_2 Swan[10, 11]	50%
C_2 Ballik-Ramsay[10–13]	50%
C_2 Phillips[10, 11]	50%
C_3 Swings[14–16]	$O(1)$ mag.
C_3 UV[14–16]	$O(1)$ mag.
C_2H UV[14–16]	$O(1)$ mag.
H_2 Lyman[17–19]	10%
H_2 Werner[17–19]	20%

2.2.1 Molecular Band Systems for Ablation Products

As will be shown in the following sections, ablation products provide significant absorption of the incoming radiative flux. For strongly radiating cases where the radiative flux drives the ablation rates, such as for a Mars return, the prediction of this absorption represents a significant component of the coupled radiation and ablation solution. This section reviews the choice of the ablation product oscillator strengths and assigns an uncertainty to value. This uncertainty will be applied in the next section, which will present an sensitivity analysis using these uncertainties as the parameter limits.

Recent reviews of molecular band system data for a CO_2-N_2 gas [10–13] provide valuable insight into the uncertainties for many of the bands systems resulting from diatomic ablation products. Comparisons between experimental measurements and various predictions for the oscillator strengths for the C_2 and CO molecules are made in these papers. These comparisons are used to determine the uncertainties applied in the present work for C_2 and CO, which are listed in Table 1. Note that these uncertainties are relatively large and range from 15 to 50%.

One of the most significant absorbers in the ablation-contaminated boundary layer is the C_3 Swings band system. The three existing measurements of this band system [14, 15, 20] result in absorption cross sections with peak magnitudes within 50% of each other (if the updated thermodynamic data is applied when backing out the cross-section [21]). However, these measurements were all for temperatures below 4000 K, and the wavelength span of each measured cross-section varied significantly. Because of these two factors, the C_3 Swings absorption cross section was assigned a one order-of-magnitude uncertainty in this analysis.

The C_3 UV band system has been measured by Shinn [16] and computed by Arnold et al. [22]. The measurements by Shinn are roughly an order-of-magnitude greater than the predictions of Arnold et al. Because of this, the C_3 UV absorption cross section was assigned a one order-of-magnitude uncertainty in this analysis.

The C_2H UV band system has been measured by Shinn [16] and Prakash et al. [15]. The influence of Mie scattering on the interpretation of these data has been questioned by Arnold et al. [22]. Because of this question and the scatter in the data, the C_2H UV absorption cross section was assigned a one order-of-magnitude uncertainty in this analysis.

Reviews of the H_2 Lyman and Werner band systems are provided by Fabian and Lewis [18]. They compare the oscillator strengths computed by Allison and Dalgarno [17], which are applied in the present study, with various experimental measurements. The agreement for the Lyman band is shown to be excellent, while that for the Werner band is slightly worse. Based on these comparisons, the oscillator strength uncertainties for the Lyman and Werner bands are assigned as ±10% and ±20%, respectively.

2.2.2 Radiation Modeling Uncertainty for a Mars Return

To provide insight into the the radiative heating uncertainty of the simulations presented in this work for high speed Earth entry, an uncertainty analysis is presented for a 5 m radius sphere, with a carbon-phenolic heat-shield, entering Earth at a range of velocities and a free-stream density of 3e-4 kg/m^3. This uncertainty analysis applies the ablation product uncertainties discussed in the previous section, along with a number of additional uncertainties presented in Ref. [23]. The uncertainty values resulting from this analysis are presented in Table 2 for the stagnation point radiative heating over a range of velocities. The individual components from the various radiative mechanisms are listed along with the total parametric uncertainty, which is the sum of the individual components. The positive uncertainty is listed without parenthesis, while the negative uncertainty is listed within parenthesis. The rows in this table each refer to a specific group of the uncertainty parameters: “Air: Molec. Bands” and “AP: Molec. Bands” refer to the uncertainty resulting from Air and Ablation Product (AP) molecular band oscillator strength uncertainties; “Air: Atomic Lines: $f_{i,j}$” from all air atomic line oscillator strength uncertainties; “Atomic Lines: $\Delta\lambda_{S,0}$” from all air atomic line Stark broadening width uncertainties; “Air: Atomic Photoionization” and “AP: Atomic Photoionization” from all air and ablation product atomic photoionization cross section uncertainties; “Air: Opacity Project Lines” from all Opacity Project line uncertainties; “Air: Neg. Ion Photodetach.” from all negative ion photodetachment cross section uncertainties. In addition to these uncertainties, the influence of including ionization potential lowering and photoionization edge shift, which are not included in the baseline model, are listed in the “Ion. Potential Lowering” and “Photo. Edge Shift” rows. These two rows represent simply the impact of adding these phenomena to the prediction (note that the “Ion. Potential Lowering” result represents the only flowfield parametric uncertainty treated in this study). Similarly, the Opacity Project exclusive lines (meaning the lines that are included in the Opacity

Table 2: Summary of parametric uncertainty contributors for the 5 m radius case at the stagnation point. Values not in parenthesis are the $+$ component while those in parenthesis are the $-$ component. All values are percent.

Parameter Group	11 km/s	12 km/s	13 km/s	14 km/s	15 km/s
Air: Molec. Bands	0.64(0.58)	0.11(0.11)	0.04(0.04)	0.01(0.01)	0.01(0.01)
Air: Atomic Lines: $f_{i,j}$	7.53(8.02)	7.21(7.88)	7.24(7.90)	6.91(7.43)	6.64(7.04)
Air: Atomic Lines: $\Delta\lambda_{S,0}$	7.17(8.31)	6.23(7.48)	5.97(7.25)	5.62(6.57)	5.26(5.90)
Air: Atomic Photoionization	3.88(3.99)	3.79(3.88)	3.76(3.78)	3.83(3.83)	3.89(3.88)
Air: Opacity Project Lines	9.73(0.00)	10.3(0.00)	10.6(0.00)	10.1(0.00)	9.70(0.00)
Air: Neg. Ion Photodetach.	4.48(4.48)	2.97(2.97)	2.02(2.02)	1.58(1.58)	1.26(1.26)
AP: Molec. Bands	2.86(6.02)	8.02(7.04)	10.0(7.72)	12.8(7.94)	15.1(7.20)
AP: Atomic Photoionization	0.40(0.37)	0.40(0.37)	0.38(0.35)	0.27(0.23)	0.16(0.13)
Ion. Potential Lowering	0.00(5.10)	0.00(4.45)	0.00(3.31)	0.00(3.18)	0.00(2.92)
Photo. Edge Shift	4.44(0.00)	4.79(0.00)	4.96(0.00)	5.14(0.00)	5.30(0.00)
Total	41.1(36.8)	43.8(34.2)	45.0(32.4)	46.2(30.8)	47.3(28.3)

Project but not by NIST) are not included in the baseline radiation model. The "Air: Opacity Project Lines" row therefore represents the total contribution from these lines (it is always a positive contribution).

Table 2 shows that at 15 km/s the parametric uncertainty for the stagnation-point radiative heating is +47.3% and -28.3%. The dominant uncertainty contributors at this velocity are a product of the atomic lines and ablation product molecular bands. At lower velocities, the ablation product molecular bands are seen to contribute less to the uncertainty. It is interesting to note that the positive uncertainty increases with velocity, while the negative uncertainty decreases. This is mainly a result of the ablation product molecular band systems (AP: Molec. Bands), whose positive uncertainty contribution increases significantly with velocity, but whose negative contribution only slightly varies.

The top individual uncertainty contributors for the 15 km/s case are listed in Table 3. The band systems for the C_3 and C_2H molecules are seen to contribute the top 2 uncertainties. These band systems are strong absorbers, meaning that the positive uncertainty is a result of decreasing the band oscillator strengths (representing the lower uncertainty bounds). In addition to the molecular band oscillator strength uncertainties, Table 3 shows the negative ion photodetachment uncertainty from atomic nitrogen (σ^- (N^-)), the atomic nitrogen photoionization cross sections (σ_{bf} (N, level 30)) from a specified electronic state (defined in Table 7 of Johnston et al. [23]), and the atomic line oscillator strength (f_{ij} (N)) and Stark broadening ($\Delta\lambda_{S,0}$ (N)) uncertainties from strong lines defined in Table 3 of Johnston et al. [23]. Note that all the individual lines in a single multiplet are combined in these results. It is seen that while the various molecular bands present in Table 3 combine to provide nearly the total molecular band uncertainty value in Table 2, the atomic line contributions in Table 3 combine to only a small fraction of the total values. This indicates that the many weak uncertainty contributions from the 430 lines for nitrogen and 293 lines for oxygen all contribute to the total atomic line uncertainty.

2.2.3 Radiation Modeling Sensitivities for a Mars Entry

In contrast to the Mars return uncertainty shown in the previous section to be dominated by equilibrium radiation properties, Johnston et al. [24] shows that the entry of a 15 m diameter hypersonic inflatable aerodynamic decelerator (HIAD) into Mars is strongly dependent on non-Boltzmann excitation rates. For example, the top 8 sensitivities of the radiative flux for a 7 km/s entry at a density of 1e-4 kg/m^3 are listed in Tables 4. The listed sensitivities are the percent change from the baseline radiative heating for a positive (+ΔK_f) or negative (-ΔK_f) change in the specified parameter (the magnitude of the $\pm$ change in each parameter is listed in the column labelled "Uncertainty"). This table shows that the top sensitivities are all non-Boltzmann rates involving

Table 3: Top uncertainty contributions from individual parameters for the 15 km/s case.

Rank	Parameter	Uncertainty ($\pm$%)	$\pm q_{rad}$ (%)
1	C_3 Swings	$O(1)$ mag.	9.60 (3.41)
2	C_2H UV	$O(1)$ mag.	2.39 (2.05)
3	σ^- (N^-)	100	1.26 (1.26)
4	C_2 Swan	50	0.89 (0.63)
5	f_{ij} (N) – 919.8 nm	50	0.49 (0.53)
6	CN Red	30	0.49 (0.46)
7	$\Delta\lambda_{S,0}$ (N) – 1052.6 nm	75	0.27 (0.66)
8	C_3 UV	$O(1)$ mag.	0.87 (0.02)
9	σ_{bf} (N, level 30)	20	0.44 (0.44)
10	$\Delta\lambda_{S,0}$ (N) – 1011.7 nm	50	0.39 (0.45)
11	f_{ij} (N) – 1070 nm	75	0.37 (0.45)
12	CO 4+	40	0.48 (0.31)
13	f_{ij} (N) – 999.1 nm	75	0.34 (0.37)
14	σ_{bf} (N, level 17)	20	0.32 (0.32)
15	H_2 Lyman	10	0.33 (0.21)

Table 4: Top 8 radiation modeling sensitivities for the ρ_{inf}=1e-4 kg/m^3 case.

#	Reaction	Uncertainty	$+\Delta K_f$	$-\Delta K_f$
8	$CO(X^1\Sigma^+) + M \leftrightarrow CO(A^1\Pi) + M$	1 om	47.2	-37.7
12	$CO(e^3\Sigma^-) + M \leftrightarrow CO(A^1\Pi) + M$	2 om	23.3	-5.10
41	$CO(a^3\Pi) + e^- \leftrightarrow CO(A^1\Pi) + e^-$	2 om	14.3	-0.25
2	$CN(A^2\Pi) + M \leftrightarrow CN(B^2\Sigma^+) + M$	1 om	3.85	-7.00
46	$CO(d^3\Delta) + e^- \leftrightarrow CO(A^1\Pi) + e^-$	2 om	6.73	-0.10
44	$CO(a'^3\Sigma^+) + e^- \leftrightarrow CO(A^1\Pi) + e^-$	2 om	6.54	-0.08
	$CO(A^1\Pi) \leftrightarrow CO(X^1\Sigma^+) + h\nu$	40%	1.69	-4.20
47	$CO(e^3\Sigma^-) + e^- \leftrightarrow CO(A^1\Pi) + e^-$	2 om	5.44	-0.07

the radiating states of the CO 4th Positive and CN Violet band system.

2.2.4 Radiation Transport

Radiation transport is computed in HARA using the tangent slab approximation. This widely used approximation is especially convenient for coupled radiation computations because the divergence of the radiative flux (Δq_r) and radiative flux to the surface depend only on the flow properties normal to the body. An option is included in HARA to allow the radiative flux at the surface to be computed using a ray tracing approach, while the tangent slab values for Δq_r are retained for coupling to the flow. The inaccuracies in q_r introduced by coupling the tangent slab value of Δq_r in the flowfield are second order, while the tangent slab value of q_r may differ from the ray tracing value by as much as 20% on forebody computations.

While the tangent-slab approximation is appropriate within a shock layer, because of the thinness of the shock layer relative to the characteristic body dimension (such as the nose radius), it is not appropriate in the precursor, where the gas emitted from the shock layer is approximated better with a point source than an infinite slab. To allow the tangent slab approach to be applied throughout the flowfield, including the precursor, the following modification is required to the tangent slab radiation transport computation of the radiative flux divergence:

$$\nabla q_\nu = \frac{dq_\nu^-}{dz} + \phi_\nu \frac{q_\nu^+}{dz} \tag{1}$$

Table 5: Top 8 radiation modeling sensitivities for the ρ_{inf}=5e-4 kg/m^3 case.

#	Reaction	Uncertainty	+ΔK_f	-ΔK_f
8	CO(X$^1\Sigma^+$) + M $\leftrightarrow$ CO(A$^1\Pi$) + M	1 om	4.10	-7.86
	CO(A$^1\Pi$) $\leftrightarrow$ CO(X$^1\Sigma^+$) +hν	40%	4.89	-6.58
	CO(d$^3\Delta$) $\leftrightarrow$ CO(a$^3\Pi$) +hν	50%	3.24	-3.24
	CN(B$^2\Sigma^+$) $\leftrightarrow$ CN(X$^2\Sigma^+$) +hν	15%	2.48	-2.54
2	CN(A$^2\Pi$) + M $\leftrightarrow$ CN(B$^2\Sigma^+$) + M	1 om	1.22	-3.48
	CO(X$^1\Sigma^+$) $\leftrightarrow$ CO(X$^1\Sigma^+$) +hν	50%	1.95	-2.15
12	CO(e$^3\Sigma^-$) + M $\leftrightarrow$ CO(A$^1\Pi$) + M	2 om	2.06	-0.55
41	CO(a$^3\Pi$) + e$^-$ $\leftrightarrow$ CO(A$^1\Pi$)+ e$^-$	2 om	1.42	-0.03

where q_ν^- and q_ν^+ are the wall and outward directed radiative flux, respectively. Following Stanley and Carlson [25], the correction factor ϕ_ν is written as

$$\phi_\nu = 1 - cos^2\beta \frac{0.5 - E_3(\tau_\nu sec(\beta))}{0.5 - E_3(\tau_\nu)} \tag{2}$$

where E_3 is the third exponential integral, τ_ν is the optical depth computed from the wall to the point in the precursor. The angle β is one-half of the angle subtended by the body, computed as

$$\beta = sin^{-1} \frac{R_{body} + z_s}{R_{body} + z} \tag{3}$$

where R_{body} is the characteristic radius of the body, z_s is the shock standoff, and z is the distance along the body normal. Equations 2 and 3 are applied for points in the precursor, defined as all points where $z > z_s$. Note that at $z = z_s$ the correction termed ϕ_ν is equal to one, while as z becomes large ϕ_ν goes to zero.

2.3 Influence of Radiative Cooling

The first, and most commonly treated influence, is the presence of the divergence of the radiative flux (Δq_r) in the energy equation, which provides the important “radiative cooling” effect. Because “coupled radiation” computations that include the divergence of the radiative flux in the energy equation typically assume Δq_r is zero in the free stream, the resulting decrease in the shock layer temperatures throughout the inviscid region of the flow leads to the term radiative cooling.

The most widely applied approach for approximating the impact of radiative cooling on the radiative heating was presented by Tauber and Wakefield. This approximation is written as

$$q_{r,TW} = \frac{q_{r,0}}{1 + 3.4\Gamma^{0.7}} \tag{4}$$

where

$$\Gamma = \frac{4q_{r,0}}{\rho_\infty U_\infty^3} \tag{5}$$

and $q_{r,0}$ is the uncoupled radiative flux (W/m^3) and ρ_∞ and U_∞ are the free-stream densities and velocities, respectively.

To observe the impact of radiative cooling on a flowfield and the resulting heating environement, a 3.04 m radius sphere at 14.07 km/s and a density of 3.79e-4 kg/m^3 is considered. This is the t=45 s case of the Mars return trajectory studied later in this paper.. The influence of coupled radiation on the vibrational-electronic temperature at various points in the flowfield is shown in Fig. 4 for this case. The radiative heating for the uncoupled, coupled radiation, and Tauber-Wakefield cases are compared in Fig. 5. It is seen that the radiatively cooled gas from the strongly radiating stagnation region flows downstream and reduces the temperatures in the weakly radiating downstream regions of the flow. This non-local radiative cooling effect causes correlations such as the Tauber-Wakefield approximation, which is dependent upon the local radiative flux, to underpredict the radiative cooling effect in dowstream regions. This effect is apparent in Fig. 5, especially in the wake where the Tauber-Wakefield approximation predicts very little cooling.

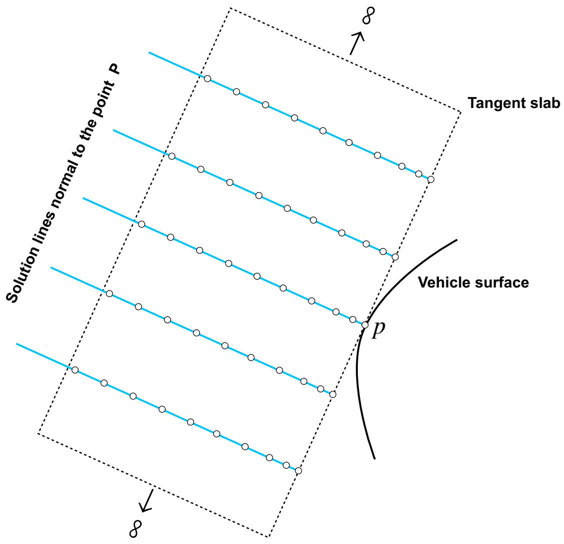

Figure 3: Schematic of the tangent slab approximation.

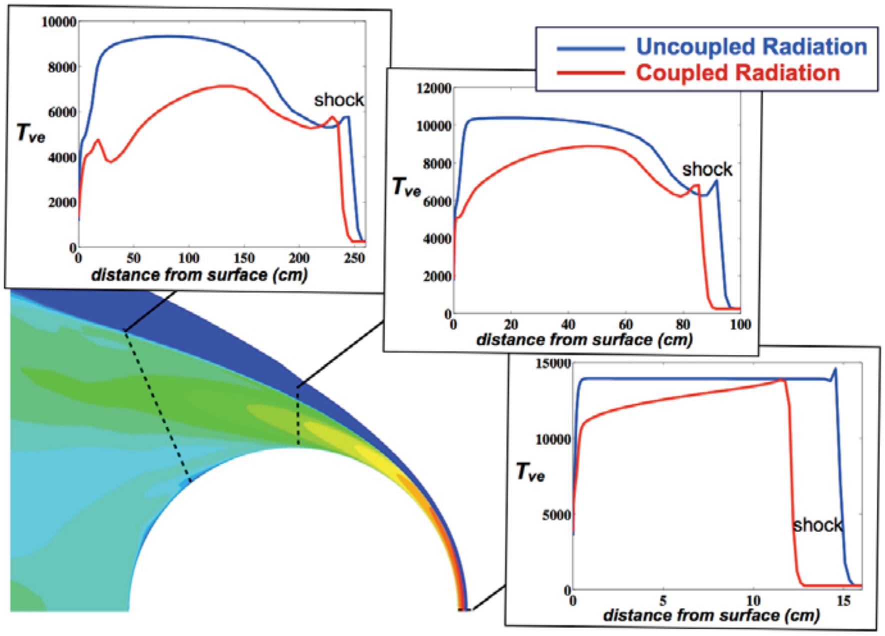

Figure 4: Temperature profiles for the Mars return case with and without coupled radiation.

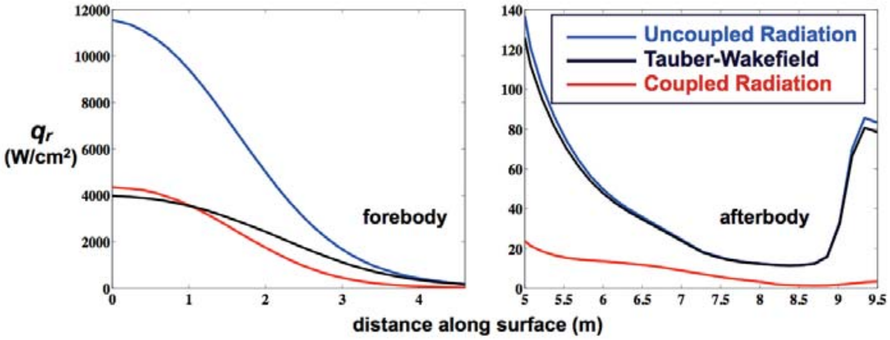

Figure 5: Radiative flux to the wall predicted with and without coupled radiation for the Mars return case.

2.4 Ablation-Radiation Interaction

For the strongly ablating shock layer typical for a Mars return entry, a strong interaction exists between the radiation and ablation, which must be properly modeled for accurate ablation or heating rate predictions. The primary source of this interaction is the strong dependence of the ablation rate on the radiative heating, while the radiative heating depends on the ablation rate through its blockage influence. While the impact of radiative heating on the predicted ablation rates will be discussed later in this paper, the influence of specified ablation rates on the radiative heating will be studied in this section.

Consider the 3.04 m radius sphere at 14.07 km/s considered in the previous section, now with a Pioneer-Venus heritage carbon phenolic heat shield. At the stagnation point, the values of $\dot{m}_c$, $\dot{m}_g$, and T_w are 0.532 kg/m^2/s, 0.074 kg/m^2/s, and 3822 K, respectively, as will be determined through a coupled analysis presented later in this paper. The resulting ablation products along the stagnation line are presented in Fig. 6, while the air species are presented in Fig. 7. The dominant ablation products are seen to be C_3 and H at the wall and C further out into the ablation layer. The temperature along the stagnation line is presented in Fig. 8, which shows the low temperature ablation layer extends roughly 2 cm from the wall. This figure also presents the non-ablating temperature profile, which is seen to be nearly identical to the ablating case, but without the ablation layer offsetting it from the wall.

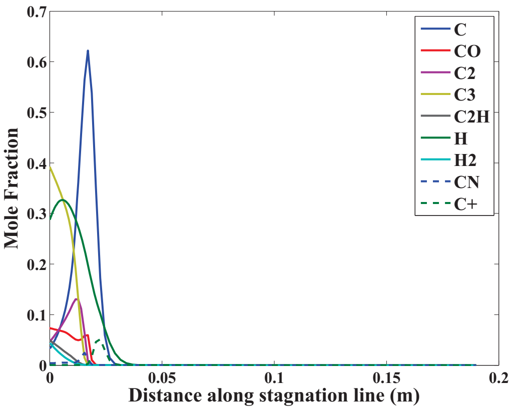

Figure 6: Mole fraction of ablation products along the stagnation line.

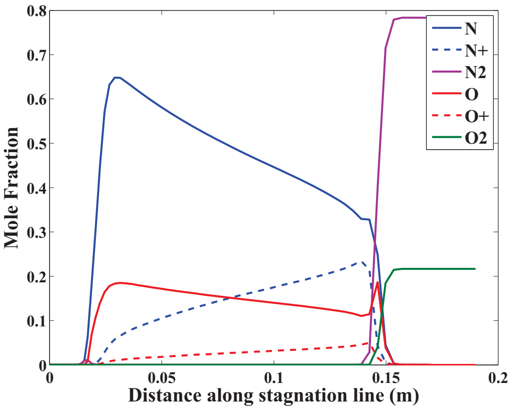

Figure 7: Mole fraction of air species along the stagnation line.

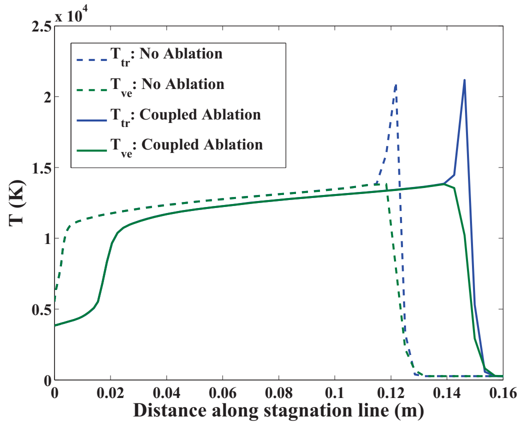

Figure 8: Comparison of non-ablating and coupled ablation temperatures along the stagnation line.

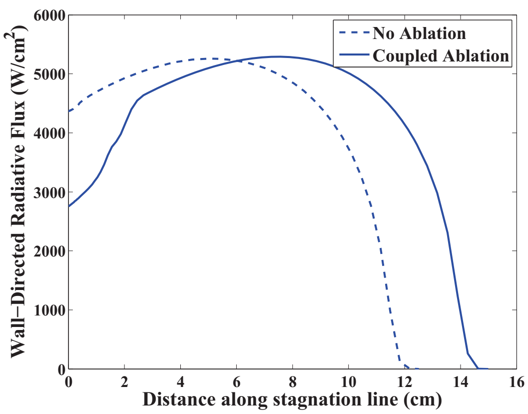

Figure 9: Comparison of non-ablating and coupled ablation radiative flux profiles along the stagnation line.

The impact of the ablation layer on the radiative flux profile along the stagnation line is shown in Fig. 9. The low temperature ablation layer is seen to provide a nearly 40% reduction in the radiative flux reaching the surface. Insight into the absorption by the ablation layer is provided by Fig. 10, which presents the spectrum at the wall for the non-ablating and coupled ablation cases. Significant absorption is apparent in three spectral regions: 2 – 4 eV, 6 – 9 eV, and above 11 eV. The transmissivity of a 1.5 cm layer of equilibrium ablator gas at 4000 K and 0.75 at, which replicates the ablation layer of the present case, is presented in Fig. 11. This allows the absorption mechanisms of the three spectral regions to be identified as the C_3 Swings band system for 2 – 4 eV, the C_3 and C_2H UV band systems for 6 – 9 eV, and atomic photoionization of C for above 11 eV. Significant uncertainties exist for the absorption coefficients of the C_3 and C_2H band systems, as were shown in Section 2.2.1, which provide the significant uncertainty contributions shown in Section 2.2.2.

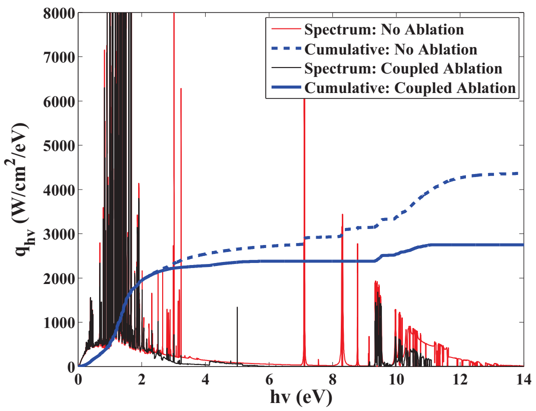

Figure 10: Comparison of non-ablating and coupled ablation radiative flux spectrum at the stagnation point.

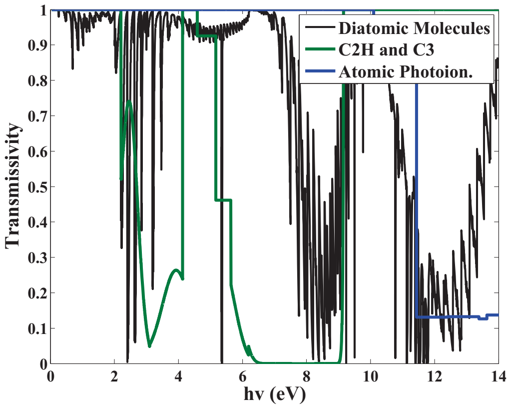

Figure 11: Transmissivity of a 1.5 cm slab of ablator gas at 4000 K and 0.75 atm.

To show impact of ablation-radiation interaction downstream of the stagnation point and in the wake region, the 14.07 km/s case is considered with an afterbody assumed to be non-ablating, radiative equilibrium, and fully-catalytic to homogenous recombination. The assumption of a non-ablating afterbody allows the influence of forebody ablation products on the afterbody to be clearly identified. The resulting mass fractions of CO and C predicted throughout the flowfield are shown in Fig. 12. This figure shows that although both CO and C are formed as a result of the forebody ablation products, they flow into the low pressure wake and dominate the species composition near the body. The influence of ablation on the radiative heating is shown in Fig. 13. On the forebody, a reduction in the radiative heating similar to that shown for the previous case is seen, while the forebody shows a surprising increase in the radiation with the introduction of ablation. This increase is a result of emission from the CO 4th Positive band system, whose contribution to the radiative flux in the wake is non-negligible because of the large CO concentration in that region.

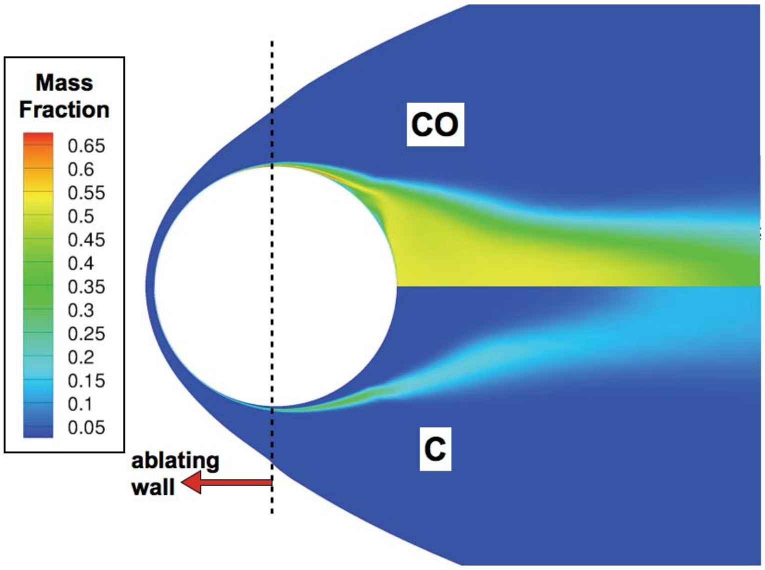

Figure 12: Mass fraction of two dominant ablation products, CO and C, for the Mars return case with coupled ablation and radiation.

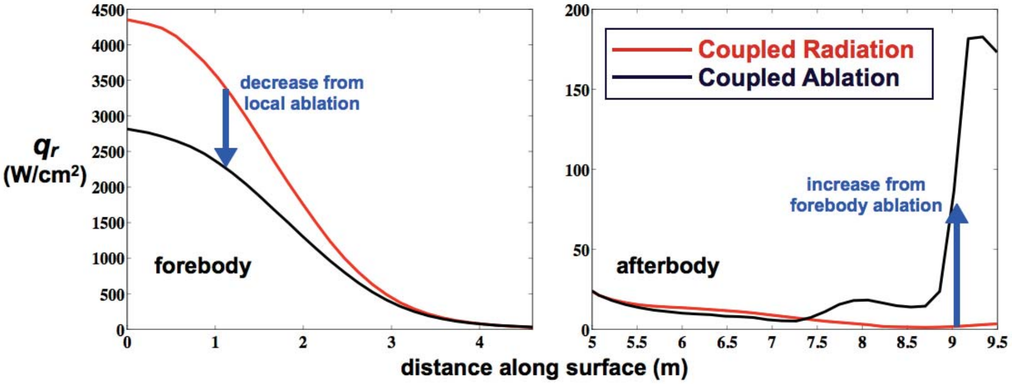

Figure 13: Radiative flux to the wall predicted with and without coupled ablation for the Mars return case.

Table 6: Photochemical Processes Applied in the Present Study.

#	Process		Spectral Range	Data Source
1	N_2 Photodissociation:	$N_2 + h\nu \leftrightarrow 2N$	9.8 eV $< h\nu$	Stanley and Carlson[25]
2	O_2 Photodissociation:	$O_2 + h\nu \leftrightarrow 2O$	7.1 eV $< h\nu$	Romanov et al.[26]
3	N_2 Photoionization:	$N_2 + h\nu \leftrightarrow N_2^+ + e^-$	12.4 eV $< h\nu$	Romanov et al.[26]
4	O_2 Photoionization:	$O_2 + h\nu \leftrightarrow O_2^+ + e^-$	9.7 eV $< h\nu$	Romanov et al.[26]
5	N Photoionization:	$N + h\nu \leftrightarrow N^+ + e^-$	12.4 eV $< h\nu$	Romanov et al.[26]
6	O Photoionization:	$O + h\nu \leftrightarrow O^+ + e^-$	9.7 eV $< h\nu$	Romanov et al.[26]

Table 7: Photochemical Source Terms Applied in the Present Study.

Species Production Rates
$\dot{w}_{photo,N_2} = -\dot{w}_{photo1} + \dot{w}_{photo,3}$
$\dot{w}_{photo,N} = 2\dot{w}_{photo,1} - \dot{w}_{photo,5}$
$\dot{w}_{photo,N_2^+} = \dot{w}_{photo,3}$
$\dot{w}_{photo,N^+} = \dot{w}_{photo,5}$
$\dot{w}_{photo,O_2} = -\dot{w}_{photo,2} + \dot{w}_{photo,4}$
$\dot{w}_{photo,O} = 2\dot{w}_{photo,2} - \dot{w}_{photo,6}$
$\dot{w}_{photo,O_2^+} = \dot{w}_{photo,4}$
$\dot{w}_{photo,O^+} = \dot{w}_{photo,6}$
$\dot{w}_{photo,e^-} = \dot{w}_{photo,3} + \dot{w}_{photo,4} + \dot{w}_{photo,5} + \dot{w}_{photo,6}$

2.5 Influence of Precursor Photochemistry

The second fundamental influence of radiation on a shock layer flowfield becomes apparent if the Δq_r computation is carried into the free-stream. For strongly radiating shock layers, the presence of Δq_r outside of the shock layer leads to significant increase in the temperature of the gas entering the shock layer. This “precursor” phenomenon is caused by photoionization and photodissociation

The radiative absorption in the precursor region is dominated by the processes of photodissociation and photoionization, which occur in the vacuum ultraviolet region of the spectrum. These processes, as applied in the present study for air, are listed in Table 6, and the absorption cross-sections were obtained from the source cited. The absorption and emission from each process were accounted for in both the radiation transport computation and the flowfield species conservation equations.The mass production rate of species n due to the photochemical process i may be written as

$$\dot{w}_{photo,i} = -m_n \int_0^\infty \frac{4\pi j_{\nu,i} - \kappa_{\nu,i} \int_{4\pi} I_\nu d\Psi}{h\nu} d\nu \tag{6}$$

where $\kappa_{\nu,i}$ and $j_{\nu,i}$ represent the absorption and emission coefficients resulting from the photochemical process i. The radiative intensity I_ν in this equation accounts for all radiative mechanisms. The production term for each species is listed in Table 7.

In addition to the processes listed in Table 6, there are several radiative transitions that influence the precursor that do not result in dissociation or ionization. These include the N_2 VUV band systems listed by Johnston et al. [27], which provide significant absorption from the ground state to the high electronic states of N_2. The O_2 Schumann-Runge band system, which lies in the 2.6 - 7.0 eV range, is found to actually emit significantly from the precursor region if a Boltzmann distribution of electronic states is assumed.

The purpose of this section is to investigate the influence of free-stream radiative absorption on the flowfield structure and associated aerothermodynamic environment at hyperbolic Earth entry conditions. The study of this effect, typically referred to as the precursor effect, has been the subject of several previous studies for air shock layers.[25, 28–34] Some of these studies [28–30, 32, 33] assumed thermochemical equilibrium throughout the shock layer and precursor region, which implies a single temperature model and chemical equilibrium throughout the flowfield. Radiation influences a thermochemical equilibrium flowfield through the presence of the divergence of the radiative flux in the energy equation. This is the term commonly treated in "coupled radiation" flowfield computations [35, 36] for both thermochemical equilibrium and nonequilibrium flowfields. A number of studies [25, 31, 34] have applied thermochemical nonequilibrium models throughout the shock layer and precursor region. The influence of radiation on these nonequilibrium flowfields is accounted for through not only the divergence of the radiative flux, but also through the photochemical production term in the species continuity equations. This term is required to treat the creation and destruction of species through photodissociation and photoionization. The work of Stanley and Carlson [25] represents the most recent detailed study of this phenomenon. They studied nitrogen flowfields using a viscous shock layer analysis. Details of the photochemical production terms was provided as well as modifications required for the tangent slab radiation transport in the precursor region. To examine the potential impact of the precursor effect on Mars-return cases, the photochemical production terms were added to LAURA following the approach of Stanley and Carlson. The absorption cross sections for the photoionization and photodissociation of O_2, which were not treated by Stanley and Carlson, were taken from Romanov et al.[26]. The cross sections for N_2 applied by Stanley and Carlson were applied here, while the photoionization cross sections for N and O were taken from the TOPbase [37].

The 15 km/s, 5 m radius Mars-return case was studied using the precursor treatment discussed in the previous paragraph. To simplify the analysis, ablation coupling is not included in these results. The vibrational-electronic temperature throughout the flowfield is presented in Fig. 14. A vibrational-electronic temperature greater than 1,000 K is seen to extend about one body radius from the surface around the sphere. In the stagnation region, this temperature nearly reaches the post-shock level as the shock is approached. This is shown more clearly in Fig. 15, which presents the stagnation line temperature profiles. In this figure, the bow shock is at 0.2 m on the horizontal axis. The vibrational-electronic temperature is seen to approach 13,000 K just before the shock, while the translational-rotational temperature remains at the free-stream value. The density is too low in the precursor region for the energy relaxation terms to begin to equilibrate the two temperatures. The divergence of the radiative flux therefore influences only the vibrational-electronic temperature.

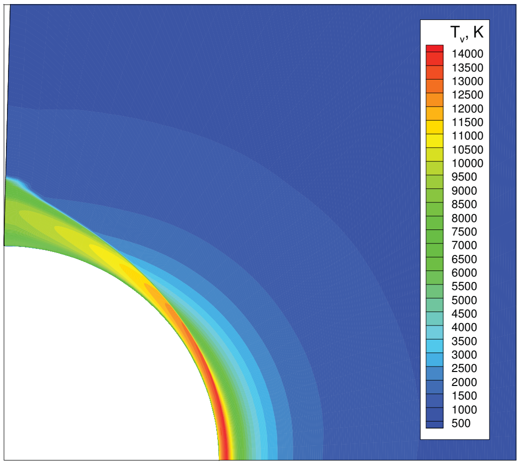

Figure 14: Vibrational-electronic temperature in the flowfield, including the precursor, for the 15 km/s, 5 m radius case.

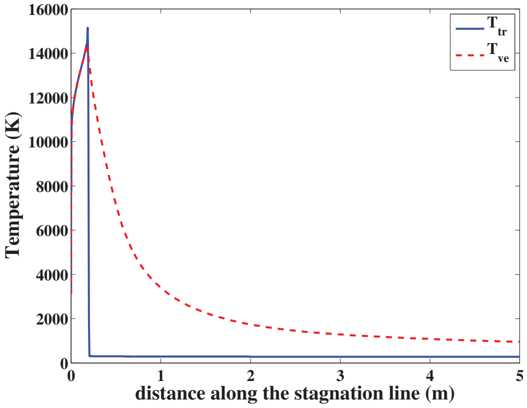

Figure 15: Temperatures along the stagnation line, including the precursor, for the 15 km/s, 5 m radius case.

The O_2 mass fraction throughout the flowfield is presented in Fig. 16. The shock layer is identified as the completely dissociated region near the body. In the stagnation region, the precursor influence is seen to reduce the O_2 mass fraction entering the shock layer from the ambient value of 0.24 to roughly 0.15. The reduction in O_2 in the precursor is due primarily to photodissociation, although O_2 photoionization is not negligible. The influence of photoionization and photodissociation may be seen in Fig. 17, which presents the species number densities along the stagnation line. The dissociation of O_2 into O is clearly seen, while the dissociation of N_2 is indicated by the rise of N. The precursor influence reduces the N_2 mass fraction entering the shock layer from 0.76 to only about 0.74 in the stagnation region, which is much less dissociation than that seen for O_2. The influence of photoionization processes are indicated by the presence of ionized species in the precursor. The most abundant ion in the precursor is seen to be O_2^+, which is followed surprisingly by NO^+. Note that collisional chemical reactions are responisble for the creation of NO and NO^+ in the precursor. These collisional reactions also have a influence on other species, although it is typically overshadowed by the photochemical contribution. The contribution of collisional reactions to the precursor is sensitive to the lower temperature limits applied to compute the forward and backward kinetic rates. Many of these rates are dependent on only T_{tr} (instead of T_{ve}), which remains near the free-stream value throughout the precursor. The validity of these rates at low temperatures (<300 K) is typically not an issue for hypersonic simulations, and therefore requires further study.

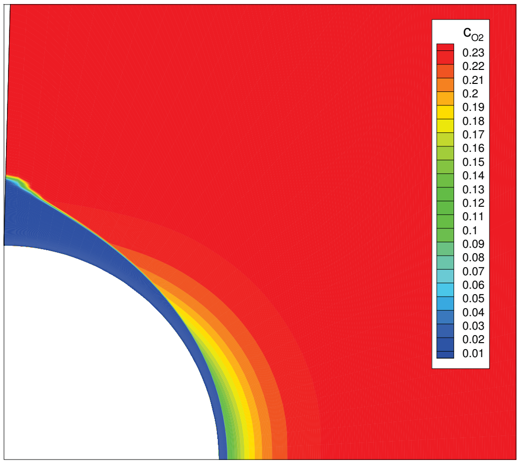

Figure 16: Mass fraction of O_2 in the flowfield, including the precursor, for the 15 km/s, 5 m radius case.

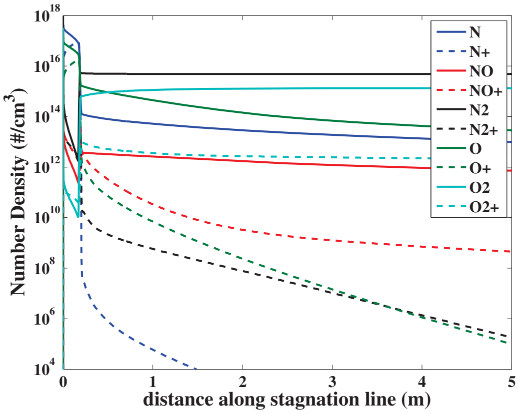

Figure 17: Number densities along the stagnation line, including the precursor, for the 15 km/s, 5 m radius case.

The strong precursor influence on the flowfield temperature and number densities shown in Figs. 14 - 17 is a result of strong radiative absorption in the free-stream. The magnitude of this absorption is indicated in Fig. 18, which presents the free-stream directed intensity profile along the stagnation line. The emission from the shock layer is apparent below 0.2 m on the horizontal axis, while beyond this point the negative slope of the curve represents absorption in the precursor. Figure 19 presents the intensity spectrum at the shock (red curve) and outer free-stream boundary (blue curve). The difference between these curves represents the total precursor absorption. It is clear that this absorption occurs exclusively in the vacuum ultraviolet (VUV) region of the spectrum ($h\nu > 6$ eV). Note that nearly all of the VUV radiation emitted from the shock layer is absorbed in the precursor.

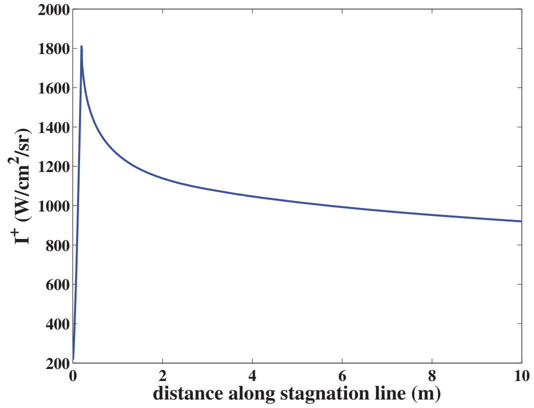

Figure 18: Radiative intensity directed along the stagnation line away from the body for the 15 km/s, 5 m radius case.

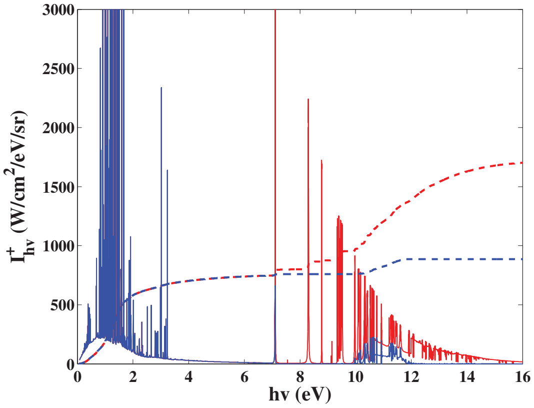

Figure 19: Radiative intensity spectrum directed away from the body at the shock (red) and outer boundary (blue).

The primary reason for modeling the precursor is to account for its influence on the shock layer radiative heating, which is strongly dependent on the shock layer temperatures. Figure 20 compares the vibrational-electronic temperature for a case with and without the treatment of the precursor (the figure is focused on the shock-layer, the rest of the precursor is the same as that in Fig. 15). The temperature difference in the shock layer between the two cases is roughly 150 K. Although this difference may appear small, the radiative heating heating is extremely sensitive to the temperature: The 1% increase in the shock layer temperature results in a 15% increase in the radiative flux reaching the wall. This result is shown in Fig. 21, which compares the wall directed radiative flux for the case with and without the precursor influence. The 15% increase due to the precursor confirms the importance of this phenomenon for modeling Mars-return radiative heating.

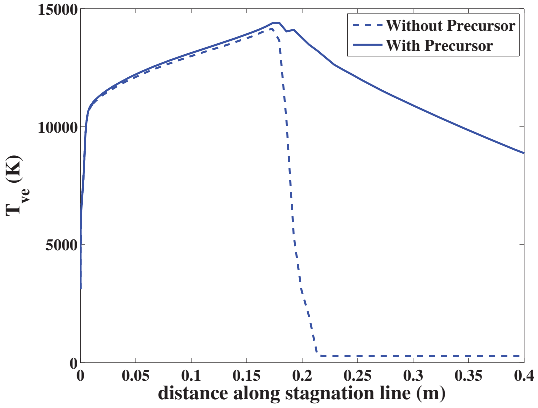

Figure 20: Vibrational-electronic temperature along the stagnation line close to the wall for the case with and without precursor modeling.

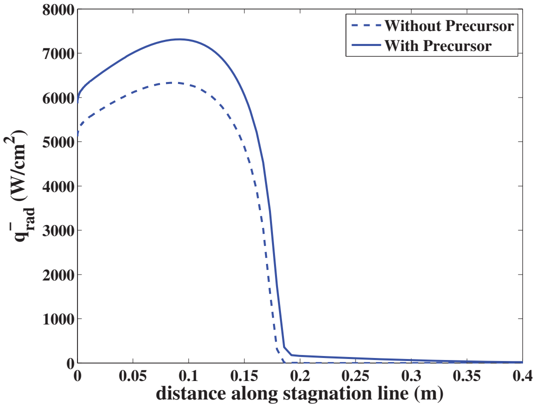

Figure 21: Wall directed radiative flux along the stagnation line close to the wall for the case with and without precursor modeling.

2.5.1 Approximate Analysis of Precursor Influence

To provide insight into the influence of precursor absorption over a wide range of nose radii and free-stream density and velocity, it is instructive to consider the flow in front of the stagnation line shock. The total energy equation may integrated from the far upstream flow (∞) to directly before the shock (s), which results in the following

$$\rho_s u_s(h_{tr,s} + h_{ve,s} + u_s^2/2) = \rho_\infty u_\infty(h_{tr,\infty} + h_{ve,\infty} + u_\infty^2/2) + Q_{rad} \tag{7}$$

To assess the impact of Q_{rad}, which is the the absorbed radiative flux along this distance, on the radiative flux reaching the vehicle surface, it is the goal of this analysis to find a simple approach for computing an equivalent velocity (U_{alt}) that provides the same enthalpy crossing the shock as a precursor solution. This equivalent velocity, which is anticipated to be slightly higher than the free-stream velocity, may then be applied as the free-stream velocity to typical non-precursor simulations, table look-ups, or curve fits of the radiative heating. From Eq. (7), U_{alt} may be written as

$$U_{alt} = \left(U_\infty^3 + \frac{2Q_{rad}}{\rho_\infty}\right)^{1/3} \tag{8}$$

To evaluate this equation, the challenge is to find a method for estimating Q_{rad} without a detailed precursor simulation. Note that Q_{rad} is written as

$$Q_{rad} = \int_{z_\infty}^{z_s} \nabla q_{r,\nu}\, dz = 2\int_0^\infty q_{\nu,s}^+ \int_{z_\infty}^{z_s} \kappa_\nu E_2 \phi_\nu dz d\nu \tag{9}$$

In this equation, $q_{\nu,s}^+$ is the radiative flux from the shock layer directed into the free-stream. The amount of this flux absorbed at each point in the free-stream is represented by $\kappa_\nu E_2 \phi_\nu$, where κ_ν is the absorption coefficient, E_2 is the second order exponential integral as a function of $z\kappa_\nu$, and ϕ_ν is defined in Eq. (2). From the application of Eq. (9) to a range of cases, it has been observed that essentially the entire VUV contribution (below 200 nm) of $q_{\nu,s}^+$ is absorbed in the precursor, and that the absorption coefficient in this range may be approximate for air with a constant: $\kappa_\nu = 30.0\rho_\infty$, where ρ_∞ has units of kg/m^3. These observations allow Eq. (9) to be simplified to the following

$$Q_{rad} = q_s^+(VUV)\left(60.0\rho_\infty \int_0^\infty \int_{z_\infty}^{z_s} E_2\phi_\nu dz d\nu\right) \tag{10}$$

where the function written in parenthesis, which is a function of $R_{body} \times \rho_\infty$, is defined as ψ, allowing Q_{rad} to be written simply as

$$Q_{rad} = q_s^+(VUV)\psi(R_{body} \times \rho_\infty) \tag{11}$$

The function ψ was curve fit to following:

$$\psi = 1 - 0.2exp(-900.0R_{body} \times \rho_\infty) - 0.8exp(-4000R_{body} \times \rho_\infty) \tag{12}$$

Equation (11) provides a convenient form for modeling the radiative flux absorbed in the free-stream. The $q_s^+(VUV)$ term, which is the wavelength integrated radiative flux directed towards the free-stream, may be taken from a non-precursor solution, while ψ is evaluated from Eq. (12). With these values, U_{alt} may be evaluated from Eq. (8) A matrix of coupled radiation cases were run for velocities, densities, and nose radii ranging from 14 – 18 km/s, 1×10^{-5} – 1×10^{-3} kg/m^3, and 0.1 – 10 m, respectively. The slope of the radiative heating with respect to free-stream velocity was found to fit the following function in this range

$$\frac{dq_r}{dU} = 4.16 \times 10^2(R_{body} + 10.48)\rho_\infty - 8.04 \times 10^{-3}(R_{body} + 7.82) \tag{13}$$

Using this relationship, the increase in the radiative heating due to precursor absorption may be computed from the following

$$\Delta q_{r,precurs} = \frac{dq_r}{dU} \times (U_{alt} - U_\infty) \tag{14}$$

The above analysis provides a convenient approach for estimating the impact of precursor absorption on the radiative heating, given the radiative heating for the non-precursor case.

3.0 COUPLED ABLATION

The primary physical phenomenon captured rigorously by a coupled ablation analysis, but approximated with varying degrees of accuracy by an uncoupled analysis, is the mixing and diffusion of ablation products through the boundary layer. For the diffusion-limited oxidation regime experienced by NASA's Orion or MSL vehicles, the recession rate is dependent upon the amount of elemental oxygen reaching the vehicle surface, which is strongly dependent on the mixing and diffusion of ablation products through the boundary layer. If the heat conducted into the surface is of primary interest instead of the recession rate, the mixing and diffusion of ablation products through the boundary layer strongly influence the diffusive flux component of the convective heating, as well as the gas enthalpy at the wall, which drive the heat conducted into the surface in the diffusion-limited oxidation regime.

Similarly, for the sublimation regime experienced by NASA's Pioneer-Venus probe, Galileo probe, or a future Mars return to Earth, the recession rate and heat conducted into the surface are strongly dependent on the radiative heating driven surface temperature. The magnitude of the radiative flux reaching the surface to drive the surface temperature, and therefore the recession rate and heat conducted into the surface, is dependent on the distribution of ablation products through the flow. These ablation products provide a layer of low temperature strongly absorbing molecules that absorb a significant fraction of the radiative heating directed towards the surface.

This section presents the details of the developed coupled ablation analysis. The basic two-temperature thermochemical nonequilibrium flowfield model discussed in Section 2.1 is applied throughout this section. The implementation of the governing surface equations for an ablating surface are presented in Section 3.1. Definitions of the three developed solution approaches, which highlight the influence of the uncoupled ablation approximations, are provided in Section 3.5.

3.1 Governing Surface Equations

The two primary governing surface equations that influence a coupled ablation solution are the surface energy balance and the elemental mass balance. The approach developed to solve these equations is described in this section.

The energy equation at the surface of a charring ablator is written as

$$q_c + \alpha q_{rad} - \epsilon \sigma {T_w}^4 - \dot{m}_c(h_w - h_c) - \dot{m}_g(h_w - h_g) - q_{cond} = 0 \tag{15}$$

The first two terms are the convective and absorbed radiative heating, which are a function of the flight condition, vehicle geometry, wall temperature, and injection of ablation products. The third term is the re-radiation from the ablator surface, which is a function of only the wall temperature and surface emissivity. The fourth and fifth terms are the enthalpy of injected char and pyrolysis gas, respectively. While h_w is the enthalpy of the gas at the wall, which is computed assuming chemical equilibrium at the surface elemental composition, temperature, and pressure, the enthalpy of the solid char (h_c) and pyrolysis gas (h_g) are typically determined experimentally and provided in table or curve-fit form for a given ablator. Finally, the heat conducted into the surface, q_{cond}, represents the inability of the previous three terms from relieving the incoming convective and radiative heat fluxes.

The elemental mass balance equation is written for each element k as

$$\dot{m}_c(\tilde{c}_{c,k} - \tilde{c}_{w,k}) + \dot{m}_g(\tilde{c}_{g,k} - \tilde{c}_{w,k}) - \tilde{J}_k = 0 \tag{16}$$

where $\tilde{c}_{w,k}$, $\tilde{c}_{c,k}$, and $\tilde{c}_{g,k}$ are the elemental compositions of the gas at the wall, char, and pyrolysis gas, respectively, and $\tilde{J}_k$ is the diffusive flux of element k. Note that the transformation from species to elements involves the identification of the fraction of element k in each species j. This is determined by multiplying the elemental weight, $\tilde{\mathrm{M}}_k$ by the number of atoms of that element in the species, $\tilde{\alpha}_{k,j}$ and dividing by the species weight M_j. Thus, the transformation from species to elemental mass fraction is achieved through the following equation

$$\tilde{c}_k = \sum_j F_{k,j} c_j \tag{17}$$

where $F_{k,j}$ is defined as

$$F_{k,j} = \frac{\tilde{\alpha}_{k,j} \tilde{\mathrm{M}}_k}{\mathrm{M}_j} \tag{18}$$

Similarly, $\tilde{J}_k$ is written as

$$\tilde{J}_k = \sum_j F_{k,j} \left(\rho D_j \frac{d\chi_j}{dz} - c_{w,j} \sum_j \rho D_j \frac{d\chi_j}{dz} \right) \tag{19}$$

where χ_j is species mole fraction, D_j is the species diffusion coefficient, and z is the distance normal to the wall.

For equilibrium ablation, the equilibrium char constraint provides an additional equation that allows $\dot{m}_c$ to be computed assuming equilibrium chemistry at the surface temperature, pressure, elemental composition. This relationship is written assuming a solid carbon char as

$$\rho_w \frac{c_{w,C}}{M_C} - K_{c,C} = 0 \tag{20}$$

where $c_{w,C}$ is the mass fraction of atomic carbon at the wall and M_C is its molecular weight. To complete the set of governing surface equations, the normal momentum equation is written as

$$\frac{dp_w}{dz} + \rho_w v_w \frac{dv_w}{dz} = 0 \tag{21}$$

which allows the the wall pressure (p_w) to be computed, with the normal velocity (v_w) obtained from the mass continuity equation:

$$\rho_w v_w = \dot{m}_c + \dot{m}_g \tag{22}$$

When combined with a equilibrium chemistry routine that computes species mass fractions and gas enthalpy for a given pressure, temperature, and elemental composition, Eqs. (15) – (22) provide the $N_{elements}$ + 4 equations required to compute $\tilde{c}_{w,k}$, T_w, $\dot{m}_c$, p_w, and v_w. The remaining unknowns in this set of equations are the pyrolysis injection rate, $\dot{m}_g$, and heat conducted into the surface, q_{cond}. These quantities depend on the time-history of $\dot{m}_c$ and T_w, as well as the material properties, such as char and virgin thermal conductivities and virgin decomposition rates. The $\dot{m}_g$ and q_{cond} are obtained in this work through an iterative procedure that feeds the $\dot{m}_c$ and T_w computed in the flowfield code through Eqs. (15) – (22) to a material response code, which computes $\dot{m}_g$ and q_{cond}.

3.2 Solution Procedure for the Governing Surface Equations

Developing a single solution procedure for Eqs. (15) – (22) stable at both the low to moderate ablating diffusion-limited oxidation regime, characteristic of an Orion ISS or MSL entry, and the massively ablating sublimation regime, characteristic of a Mars return or Galileo probe, presents a significant numerical challenge. The trial and error of many approaches over the years has lead to a simple two dimensional search algorithm.

The outer loop of this algorithm solves the energy equation, Eq. (15), for T_w while the inner loop solves the char constraint, Eq. (20), for $\dot{m}_c$.

This procedure begins by defining a upper and lower limits of T_w over which to perform the search algorithm. The upper temperature limit is set by computing the radiative equilibrium wall temperature (T_{REW}) at the local convective and radiative heating values. If T_{REW} is less than 3200 K, the upper temperature limit is set as T_{REW} + 300 K. If If T_{REW} is greater than 3200 K, the upper temperature limit is set to 4500 K. The lower temperature limit is computed simply to 30% of the input wall temperature, with a lower limit of 800 K enforced. Once the T_w limits are set, the temperature is set to the middle of the limits, This temperature is then applied to the inner loop computation for $\dot{m}_c$.

The inner loop computation increase $\dot{m}_c/(\rho_\infty U_\infty)$ in order of magnitude increments, starting from 1e-6, until the residual of the energy, f_{energy} equation changes sign. This residual is written as a modified form of Eq. (15) as follows

$$f_{energy} = q_c + \alpha q_{rad} - \epsilon \sigma {T_w}^4 - \dot{m}_c(h_w - h_c) - \dot{m}_g(h_w - h_g) - q_{cond}\frac{T_w}{T_w^0} \tag{23}$$

Because q_{cond} is provided by a material response code, it remains constant during the present iterative process. The temperature ratio placed on this term, where T_w^0 is the initial input temperature for which q_{cond} was computed, allows for an approximate temperature dependence. The temperature dependences of h_c and h_g are represented through provided tables or curve fits. The main challenge in the evaluation of f_{energy} is computing h_w, which is obtained from an equilibrium chemistry computation at the wall temperature, pressure, and elemental composition. Solving Eq. (16) for the required elemental mass fractions, for a given $\dot{m}_c$ and $\dot{m}_g$, is nontrivial because there is no explicit dependence of the elemental mass fractions on $\tilde{J}_k$. To approximate this dependence during the iteration process on $\dot{m}_c$, the following approximation is applied

$$\tilde{J}_{k,approx} = \tilde{J}_k^0(\tilde{c}_{w,k} - \tilde{c}_{e,k})/(\tilde{c}_{w,k}^0 - \tilde{c}_{e,k}) \tag{24}$$

where the superscript “0” refers to the initial input values. When applied to Eq. (16), the following explicit solution for $\tilde{c}_{w,k}$ is obtained

$$\tilde{c}_{w,k} = \frac{\tilde{c}_{e,k} + Y'_{c,k}\tilde{c}_{c,k} + Y'_{g,k}\tilde{c}_{g,k}}{1 + Y'_c + Y'_g} \tag{25}$$

where

$$Y'_{c,k} = \dot{m}_c(\tilde{c}_{w,k}^0 - \tilde{c}_{e,k})/\tilde{J}_k^0 \tag{26}$$

and

$$Y'_{c,k} = \dot{m}_g(\tilde{c}_{w,k}^0 - \tilde{c}_{e,k})/\tilde{J}_k^0 \tag{27}$$

Limits on the sum $Y'_k = Y'_{c,k} + Y'_{g,k}$ in the denominator of Eq. (25) are required to avoid values near -1, which may occur in early stages of convergence. These limits are beyond of the scope of this paper. This approach utilizing Eqs. (24) – (27) is analogous to approximate “B-prime” discussed later in this paper, which would replace $\tilde{J}_k^0$ with q_c in all these equations, and the elemental mass fractions with enthalpies in Eqs. (26) and (27). However, while the B-prime approach approximates $\tilde{J}_k$ with an equal diffusion coefficient film coefficient model, the present approach converges to the rigorous solution of Eq. (25). This convergence is achieved after numerous calls to the presently described ablation subroutine, when the computed $\tilde{c}_{w,k}$ is equal to the input value, $\tilde{c}_{w,k}^0$, which results in $\tilde{J}_{k,approx} = \tilde{J}_k^0$ in Eq. (24), therefore removing any diffusion approximation.

Once an order of magnitude range of $\dot{m}_c$ is determined over which f_{energy} changes sign, a simple bisection approach is applied over this range to determine the $\dot{m}_c$ that results in $f_{energy} = 0$. Once this $\dot{m}_c$ is found, the corresponding species density and atomic carbon mass fraction are applied to the char constraint of Eq. (20). This equation is written in terms of a residual, f_{char}, as follows

$$f_{char} = \rho_w \frac{c_{w,C}}{M_C} - K_{c,C} \tag{28}$$

where $K_{c,C}$ is evaluated through a curve fit at T_w. Analysis of this equation allows the f_char values at the lower and upper temperature limits chosen for this search algorithm to be set to 1e+10 and -1e+10, respectively. With these values set, the f_{char} computed at T_w replaces the limit with an opposite sign of f_{char}, and a new T_w is chosen as the midpoint between these new limits. The inner loop computation of $\dot{m}_c$ is then repeated at the new T_w and the process repeats itself until f_{char} is near zero.

A complication to the above procedure arises when the $\dot{m}_g$, provided by the material response code, is large enough to repress $\dot{m}_c$ to a value of zero. Such a situation is checked for each T_w iteration by evaluating Eqs. (24) – (27), along with the corresponding equilibrium chemistry, with $\dot{m}_c$ set to zero. If the resulting $f_{char} > 0$, then $\dot{m}_c$ is set to zero and the inner loop of the search procedure bypassed. However, because f_{char} was used to set $\dot{m}_c$ to zero, the outer loop bisection search for T_w applies f_{energy} instead of f_{char}.

3.3 Steady State Ablation Approximation

For the present study, $\dot{m}_g$ and T_w are either specified from a material response code or obtained using the steady-state ablation approximation. The steady-state ablation approximation requires the solution of an approximate surface energy equation:

$$-q_c - \alpha q_{rad} + \epsilon\sigma {T_w}^4 + (\dot{m}_c + \dot{m}_g)h_w = 0 \tag{29}$$

which assumes that the char surface and virgin material recede at the same linear rate. The steady-state ablation approximation provides the following relationship for $\dot{m}_g$:

$$\dot{m}_g = (\frac{\rho_v}{\rho_c} - 1)\dot{m}_c \tag{30}$$

It will be stated whenever this approximation is applied through this work. Note that it is convenient for cases where a time history of the heating environment required for a material response code is not available.

3.4 Uncoupled Ablation Approximations

The assessment and design of reentry heatshields typically involve an uncoupled ablation-flowfield analysis. This uncoupled analysis consists of applying a non-ablating flowfield prediction, which defines the heat-transfer coefficient, wall enthalpy and wall pressure, to an equilibrium ablation model, which computes $\dot{m}_c$, $\dot{m}_g$, T_w, and in-depth material properties. The analysis is referred to as "uncoupled" because the influence of $\dot{m}_c$, $\dot{m}_g$, and T_w on the flowfield prediction are treated approximately within the ablation model, and hence the ablation model is not coupled with the flowfield model. For diffusion-limited oxidation cases, the prediction of $\dot{m}_c$ is sensitive to the treatment of $\tilde{J}_k$, while for the sublimation regime it is sensitive to q_c and the surface energy balance. For the uncoupled ablation analysis, two fundamental approximations are applied to model the influence of $\dot{m}$ on $\tilde{J}_k$ and q_c. These are defined as follows:

1. *Approximation #1*:

   The influence of $\dot{m}_c$ and $\dot{m}_g$ on the heat-transfer coefficient is approximated as

$$C_H = C_{H,0} \frac{2\lambda B_0}{exp(2\lambda B_0) - 1} \tag{31}$$

where $C_{H,0}$ is the non-abating heat-transfer coefficient. Recall that C_H is related to q_c as

$$q_c = C_H(H_T - h_w) \tag{32}$$

This approximation has been assessed by Thompson and Gnoffo[38] and Martinelli et al.[39] for perfect gas flows.

2. *Approximation #2*:

   The elemental diffusion mass flux at the surface is written as[40]

   $$\tilde{J}_k = C_M(\tilde{c}_{w,k} - \tilde{c}_{e,k}) \tag{33}$$

   where it is assumed that $C_M = C_H$. This approximation allows the elemental mass balance at the wall to be solved algebraically for the elemental mass fractions at the wall: [40]

   $$\tilde{c}_{w,k} = \frac{\tilde{c}_{e,k} + B'_c\tilde{c}_{c,k} + B'_g\tilde{c}_{g,k}}{1 + B'_c + B'_g} \tag{34}$$

   A discussion of this approximation is presented by Bianchi et al.[41] for graphite ablation.

3.5 Definitions of Applied Approaches

To make clear the influence of Approximations #1 and #2, solutions will be presented that include both approximations, only Approximation #1, and neither approximation. These three different approaches are defined as follows:

1. *Uncoupled*: This approach applies both approximations, and is identical to the typical “uncoupled” approach applied in heatshield design. It is applied as a post-processing step to a non-ablating solution, obtained assuming a super-catalytic, radiative equilibrium wall. The non-ablating solution provides $q_{c,0}$, h_w, and p_w. The solution procedure described in Section 3.2 is applied with two modifications. First, the q_c applied in the energy equation is computed using $q_{c,0}$ and Approximation #1. Second, Eq. 25 is replaced by Eq. 34, representing Approximation #2. Note that this approach is identical to the application of B’ tables often applied in material response codes, although the present approach does not actually apply any pre-computed tables.

2. *Partially-Coupled*: This approach removes Approximation #1, but contains Approximation #2. It consists of a flowfield with coupled ablation, meaning that the injection of ablation products is treated in the flowfield solution. Therefore, Approximation #1 is not applied because the influence of $\dot{m}$ on C_H is explicitly treated. However, this approach retains Approximation #2, meaning that Eq. 25 is replaced by Eq. 34 in the solutions procedure described in Section 3.2.

   The application of this approach typically begins by first obtaining a non-ablating flowfield solution. From this, the procedure outlined in the Section 3.2 (with Eq. 25 replaced by Eq. 34) to obtain $\dot{m}_c$, T_w, and $c_{w,i}$ is called every 5,000 – 50,000 flowfield iterations, depending on the magnitude of the injections rates. In between these surface computations, the pseudo-cells at the wall are updated every 50 flowfield iterations to maintain the computed surface properties, which are assumed equal to the average of the pseudo-cell values and the values in the first cell above the wall. This procedure is very robust and converges for a wide range of ablation rates.

3. *Fully-Coupled*: The solution approach described in Section 3.2 is applied directly as written, therefore avoiding the use of both Approximations #1 and #2. This approach provides the most rigorous possible application of equilibrium ablation.

   As with the Partially-Coupled approach, it is convenient to begin the solution procedure with a converged non-ablating flowfield solution. The $\dot{m}_c$ and T_w values are then computed using the procedure described in Section 3.2. An important step in this procedure is the updating of the elemental and species mass fractions at the wall for the given $\dot{m}_c$, $\dot{m}_g$, and T_w values. Instead of using Eqs. (24) – (27), which were required to handle the large variation in $\dot{m}_c$ encountered within the search algorithm, the pseudo cells at the wall are updated by approximating $\tilde{J}_k$ as follows

$$\tilde{J}_{k,approx} = A_1 \frac{\tilde{c}_{k,1}}{\tilde{c}^0_{k,1}} - A_0 \frac{\tilde{c}_{k,0}}{\tilde{c}^0_{k,0}} + B_1 \tilde{c}_{k,1} + B_0 \tilde{c}_{k,0} \tag{35}$$

   where

$$A_n = \sum_j F_{k,j} \rho D_j \frac{\chi_{j,n}}{\Delta z} \tag{36}$$

$$B_n = -\sum_j F_{k,j} c_{j,n} \sum_j \rho D_j \frac{(\chi_{j,1} - \chi_{j,0})}{\Delta z} \tag{37}$$

   The psuedo cell is identified by the subscript “0”, while the first cell above the wall is identified by the subscript “1” (the superscript “0” refers to the initial input values, as before). The distance between the cell centers is Δz. Substituting this relationship into Eq. (16) allows $\tilde{c}_{k,0}$ to be solved algebraically for the given $\dot{m}_c$ and $\dot{m}_g$. Updates to the surface using this approach are made every 2 - 5 flowfield iterations, which allows the chemistry at the wall to evolve to the appropriate values for the given $\dot{m}_c$, $\dot{m}_g$, and T_w. Once this is achieved after every 5,000 – 50,000 flowfield iterations, depending on the magnitude of the injections rates, the ablation routine described in Section 3.2 is called for new $\dot{m}_c$ and T_w values.

3.6 Earth Entry Case at 6 km/s

3.6.1 Analysis of 6 km/s Earth Entry Case with Fixed Ablation Rates

To evaluate the differences between the Uncoupled, Partially-Coupled, and Fully-Coupled approaches defined in Section 3.5, cases with specified $\dot{m}_c$, $\dot{m}_g$, and T_w are studied here for each approach. The validity of Approximation #1 is assessed by comparing the C_H values predicted by the Uncoupled and Partially-Coupled approaches. Recall that C_H is computed from Eq. (31) for the Uncoupled approach, which represents Approximation #1, while it is computed directly from Eq. (32) for the Partially-Coupled approach. If the C_H values agree between the Uncoupled and Partially-Coupled approaches, then Eqs. (33) and (34) will predict the same $\tilde{c}_{w,k}$ values at the surface (because B'_c and B'_g will be identical and C_M = C_H). Thus, if $\dot{m}_c$ was to be computed from Eq. (20) instead of held fixed (as will be done in the next section), then the

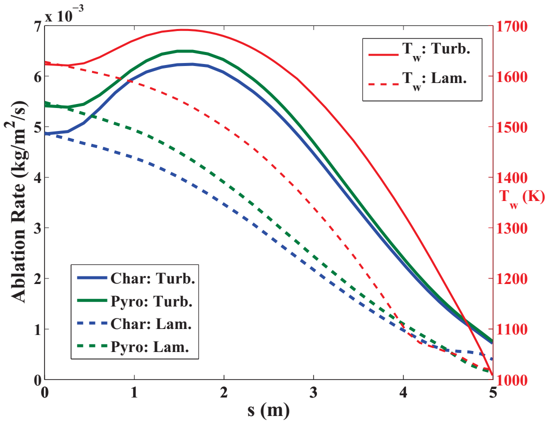

Figure 22: Specified ablation rates and wall temperature.

Table 8: Comparison of Uncoupled, Partially-Coupled, and Fully-Coupled approaches with fixed $\dot{m}$ and T_w at the stagnation-point.

Approach	q_c (W/cm^2)	C_Hx10^2 (kg/(m^{2}s))	$\tilde{c}_{w,C}$	$\tilde{c}_{w,O}$	$\tilde{c}_{w,H}$	$c_{w,C}$
Uncoupled	38.0	2.11	0.171	0.263	1.62e-2	4.1e-17
Partially-Coupled	34.6	1.92	0.181	0.264	1.71e-2	3.2e-16
Fully-Couped	36.4	1.94	0.205	0.322	1.02e-2	8.2e-19

Uncoupled and Partially-Coupled approaches would predict the same $\dot{m}_c$. However, if the predicted C_H values differ, then the predicted $\dot{m}_c$ would be expected to differ accordingly. Generally, a larger C_H translates to a larger $\dot{m}_c$.

The validity of Approximation #2 is assessed by comparing the $\tilde{c}_{w,k}$ values predicted by the Partially-Coupled and Fully-Coupled approaches. Recall that Approximation #2 is the only difference between these two approaches. For a given temperature and pressure, the $\tilde{c}_{w,k}$ values define the atomic carbon mass fraction at the wall ($c_{w,C}$). The $c_{w,C}$ values are of interest because they are present in the char equilibrium constraint of Eq. (20), which will be applied in the next section to compute $\dot{m}_c$. Generally, a larger $c_{w,C}$ in the present analysis will translate to a smaller $\dot{m}_c$ in the computed–$\dot{m}_c$ analysis of the next section. It will be convenient to compare $\tilde{c}_{w,k}$ values, as they provide a compact means for interpreting the chemical composition at the surface. Typically, larger values of $\tilde{c}_{w,C}$ are associated with larger values of $\tilde{c}_{w,O}$, because CO is the dominant species (along with N_2) at the surface. The lower the $\tilde{c}_{w,O}$ value, the less CO that can be formed, and the more $\tilde{c}_{w,C}$ that is available for forming atomic carbon.

The elemental mass fractions applied in this study for Avcoat are taken from Bartlett [42], and are equal to: [C, H, O, N, Si] = [0.49, 0.00, 0.27, 0.00, 0.24] for the char and [C, H, O, N, Si] = [0.55, 0.09, 0.34, 0.02, 0.00] for the pyrolysis gas.

The present analysis was applied to a 3.6 m radius sphere at a free-stream velocity and density of 6.0 km/s and 3.0e-4 kg/m^3, respectively. The specified ablation rates and wall temperatures along the body are shown in Fig. 22. So that these specified values would have reasonable profiles and magnitudes, they were obtained assuming steady-state ablation and using the Partially-Coupled approach. For the laminar case, the resulting stagnation-point surface properties predicted using the Uncoupled, Partially-Coupled, and Full-Coupled approaches are listed in Table 8. As mentioned previously, the influence of Approximation #1 is seen by comparing the C_H values predicted by the Uncoupled and Partially-Coupled approaches. Table 8 shows that the Uncoupled C_H is 10% larger than the Partially-Coupled value. This indicates that the Uncoupled approach will likely predict, for the computed–$\dot{m}_c$ analysis presented in the next section, a larger $\dot{m}_c$ than the Partially-Coupled approach. Also mentioned previously, the influence of Approximation #2 is seen by comparing the $\tilde{c}_{w,k}$ values predicted by the Partially-Coupled and Fully-Coupled approaches. Table 8 shows that the Parially-Coupled $\tilde{c}_{w,C}$ value is 10% smaller than the Fully-Coupled value, while the $\tilde{c}_{w,O}$ value is roughly 20% smaller. The larger amount of oxygen relative to carbon for the Fully-Coupled approach results in less atomic carbon at the wall, as seen in the last column of Table 8. For the computed–$\dot{m}_c$ analysis, this indicates that the Fully-Coupled approach will likely predict a larger $\dot{m}_c$ than the Partially-Coupled approach. Note that this analysis suggests that Approximations #1 and #2 will have offsetting influences in the computed–$\dot{m}_c$ analysis when comparing the Uncoupled and Fully-Coupled $\dot{m}_c$ values.

The trends mentioned in the previous paragraph for the stagnation-point, are shown to be true downstream of the stagnation point. The Uncoupled and Partially-Coupled C_H values along the body are compared in Fig. 23 for the turbulent and laminar cases. The C_H differences between the Uncoupled and Partially-Coupled approaches seen here for the turbulent case are not consistent with the downstream laminar results. Instead of the Uncoupled C_H being larger than the Partially-Coupled value, it is seen to be roughly 15% smaller than the Partially-Coupled value. This difference will have a significant influence on the computed $\dot{m}_c$ analysis presented in the next section. This is especially true because the trends in the $\tilde{c}_{w,k}$ values predicted by the Partially-Coupled and Fully-Coupled approaches, and compared along the body in Fig 24, are similar to the laminar case. This means that Approximations #1 and #2 will both result in $\dot{m}_c$ increases (in contrast to their offsetting increase and decrease for the laminar case).

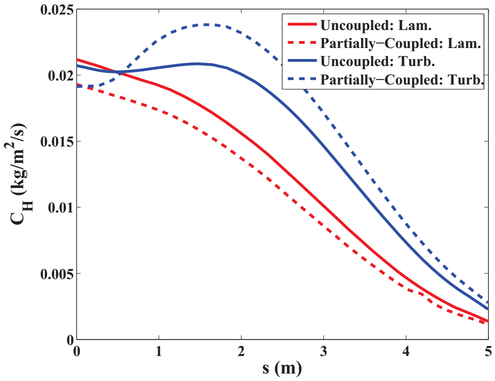

Figure 23: Predicted C_H values along the body.

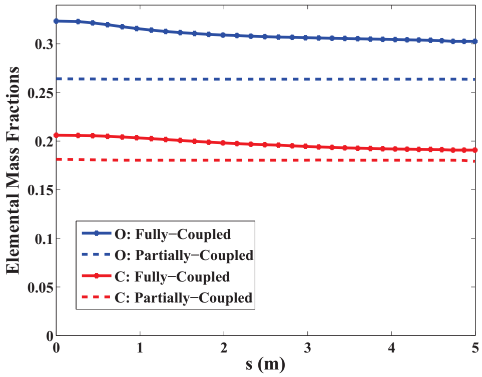

Figure 24: Predicted $\tilde{c}_{w,k}$ values along the body for the turbulent case.

The inaccuracy of Approximation #1 in turbulent regions was observed in the previous paragraph. This behavior is anticipated to have a significant influence on the computed $\dot{m}_c$ analysis presented in the next section. Therefore, it will be studied in more detail here. The non-ablating ($q_{c,0}$), Uncoupled, and Partially-Coupled q_c values are compared in Fig. 25 for the turbulent case. This figure shows that the Partially-Coupled q_c becomes nearly equal to the non-ablating value in the downstream turbulent regions. This behavior is not followed by the Uncoupled approach, which is the reason for the disagreement in the C_H values shown in Fig. 23. Note that q_c may be separated into two components, the conductive component:

$$q_{c,cond} = k_{ve}\frac{dT_{ve}}{dz} + k_{tr}\frac{dT_{tr}}{dz} \tag{38}$$

and the diffusive component:

$$q_{c,diff} = \rho \sum_{i=species} J_i h_i \tag{39}$$

These components are presented in Fig. 26 for the non-ablating and Partially-Coupled cases. It is seen that the conductive component is reduced and the diffusive component is increased with the introduction of ablation. The increase of the diffusive component at the stagnation point (therefore, not influenced by turbulence) is a result of the different chemistry near the wall for the ablating case. The larger increase of the diffusive component downstream of the stagnation point, however, is a result of turbulence. This turbulent downstream region is strongly dependent on the Sc_{turb}, and less so on the other details of the turbulence model. If Sc_{turb} is increased above the present value of 1.0, the influence of turbulent diffusion decreases. If a large Sc_{turb} value is applied to both the non-ablating (which drives the Uncoupled result) and Partially-Coupled solutions, the agreement between the Uncoupled and Partially-Coupled q_c (and C_H) values becomes significantly better.

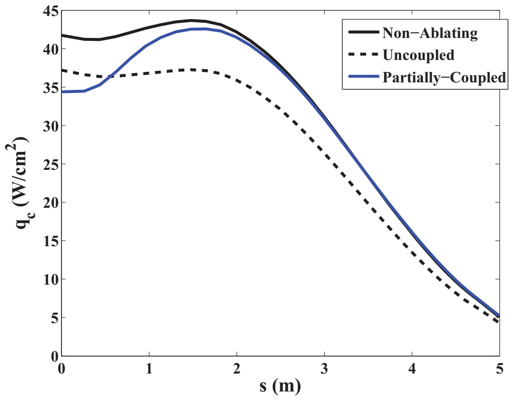

Figure 25: Comparison of q_c values along the body for the turbulent case.

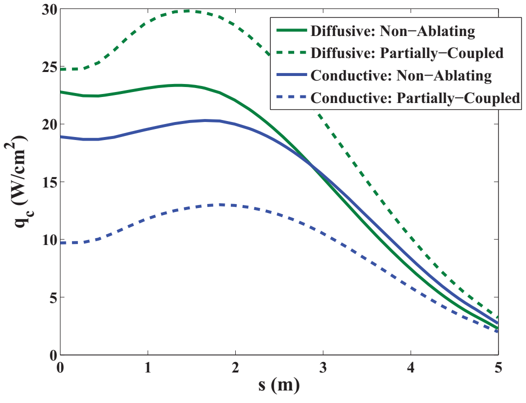

Figure 26: Comparison of the diffusive and conductive components for the turbulent case.

3.6.2 Analysis of 6 km/s Earth Entry Case with Computed Char Ablation Rates

The present section engages Eq. (20) to allow $\dot{m}_c$ to be computed as part of the flowfield solution. The differences in the $\dot{m}_c$ predicted using the Uncoupled, Partially-Coupled, and Fully-Coupled approaches are of particular interest, and are the main results of this paper. The $\dot{m}_g$ and T_w values are fixed to the same values as in the previous section. Note that the restriction of fixed T_w could be easily removed by applying Eq. (29). This was not done here to simplify the interpretation of the results, and because in the diffusion-limited regime studied here, T_w has a weak influence on $\dot{m}_c$. It is assumed that for practical applications a material response code will provide $\dot{m}_g$, and this value will likely not be sensitive to $\dot{m}_c$. Thus, holding $\dot{m}_g$ fixed in the present study is justified.

The differences in q_c, C_H, and $\tilde{c}_{w,k}$ predicted by the Uncoupled, Partially-Coupled, and Fully-Coupled approaches were presented in the previous section for fixed $\dot{m}_c$ values (with $\dot{m}_g$ and T_w also fixed). In the discussion of those results, the results of the present section were correctly anticipated, as will be shown.

The 3.6 m radius sphere at a free-stream velocity and density of 6.0 km/s and 3.0e-4 kg/m^3 considered in the previous subsection is considered here. The $\dot{m}_g$ and T_w values are fixed to those shown in Fig. 22. The resulting $\dot{m}_c$ values are presented along the body in Figs. 27 and 28 for the laminar and turbulent cases, respectively. For the laminar case, the Fully-Coupled $\dot{m}_c$ is only slightly larger than the Uncoupled result, while it is 20% larger than the Partially-Coupled result. This peculiar result that the Uncoupled approach is in better agreement (with the Fully-Coupled approach) than the Partially-Coupled approach was to be expected from Section 3.6.1, which showed that for the laminar case Approximations #1 and #2 result in offsetting errors. In other words, removing Approximation #1 causes the $\dot{m}_c$ difference seen between the Uncoupled and Partially-Coupled approaches, which for the laminar case is a 20% decrease in $\dot{m}_c$. This is a result of Approximation #1 over-predicting C_H, as was shown in Fig. 23. Similarly, removing Approximation #2 causes the $\dot{m}_c$ difference seen between the Partially-Coupled and Fully-Coupled approaches, which for the laminar case is about a 23% increase in $\dot{m}_c$.

For the turbulent results shown in Fig. 28, the comparison between approaches in the downstream region is significantly different than the laminar results. As was discussed in Section 3.6.1, in regions of turbulence Approximation #1 under-predicts C_H, which is the opposite of the laminar trend. As a result, removing Approximation #1 causes an increase in $\dot{m}_c$. The influence of Approximation #2 is the same for the turbulent case as it is for the laminar case, and therefore removing it also causes an increase in $\dot{m}_c$. Because removing Approximations #1 and #2 both provide increases in $\dot{m}_c$, instead of providing offsetting differences as in the laminar case, the difference between the Uncoupled and Fully-Coupled results is significant, with the the Fully-Coupled $\dot{m}_c$ being 49% larger than the Uncoupled value at s = 2.0 m.

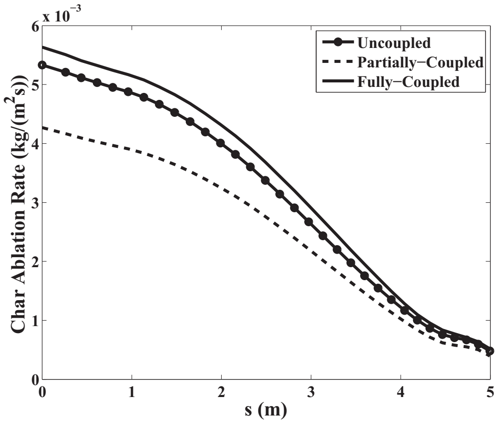

Figure 27: Predicted laminar $\dot{m}_c$ values the 6 km/s Earth entry case.

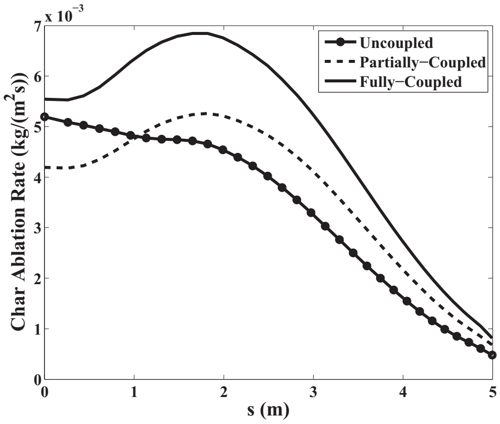

Figure 28: Predicted turbulent $\dot{m}_c$ values for the 6 km/s Earth entry case.

3.7 Mars Entry Case at 5.26 km/s

To show the influence of Approximations #1 and #2 for a Mars entry vehicle, this section presents an analysis similar to that of the previous subsection, but with a free-stream composition of 0.974 CO_2 and 0.026 N_2. A 4-m radius sphere at a velocity of 5.26 km/s and a density of 6.96e-4 kg/m^3 is considered with a solid carbon char and pyrolysis mass fraction composition of [C,H,O,N] = [0.40, 0.145, 0.435, 0.02].

For the fixed char rate, pyrolysis rate, and wall temperature shown in Fig. 29, the influence of Approximations #1 and #2 on the elemental oxygen reaching the surface is seen in Fig. 30. Similar to the behavior observed in the previous section for the Earth entry cases, the Fully-Coupled approach predicts more elemental oxygen at the surface than the Uncoupled approach for a given $\dot{m}_c$, $\dot{m}_g$, and T_w. Note that for this Mars entry case the elemental oxygen at the wall is lower than the boundary layer edge value of 0.708, while for the Earth entry case it was larger.

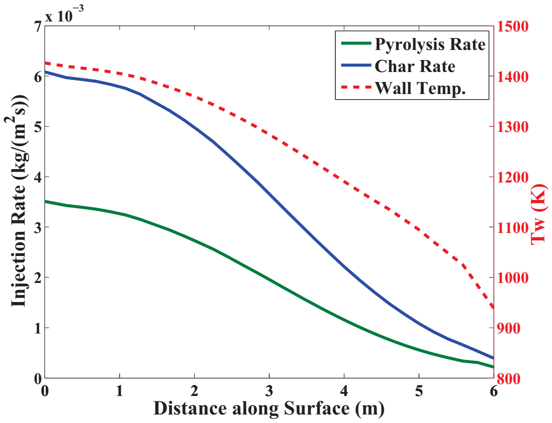

Figure 29: Specified surface values for the 5.26 km/s Mars entry case.

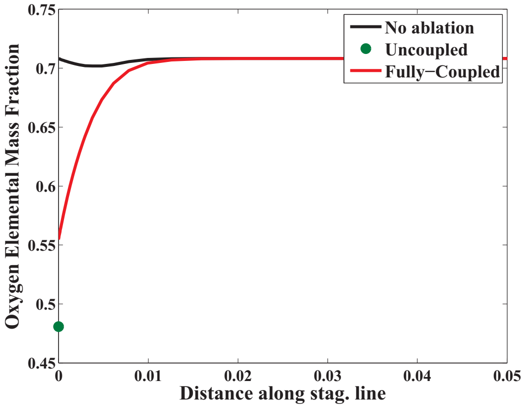

Figure 30: Elemental mass fraction of oxygen through the boundary layer for the Mars entry case with specified $\dot{m}_c$, $\dot{m}_g$, and T_w.

If the char equilibrium constraint is enforced and $\dot{m}_c$ is computed instead of specified, with $\dot{m}_g$ and T_w fixed to the values in Fig. 29, the resulting $\dot{m}_c$ values from the three approaches are presented in Figure 31. As anticipated from the larger elemental oxygen mass fraction predicted by the Fully-Coupled approach in the specified $\dot{m}_c$ analysis of the previous paragraph, the Fully-Coupled approach predicts larger $\dot{m}_c$ values than the Uncoupled approach. This 70% larger $\dot{m}_c$ at the stagnation point indicates the inadequacy of the Uncoupled approach for predicting surface recession for Mars entry cases. The corresponding convective heating is presented in Fig. 32, which does not show the same level of disagreement as the $\dot{m}_c$.

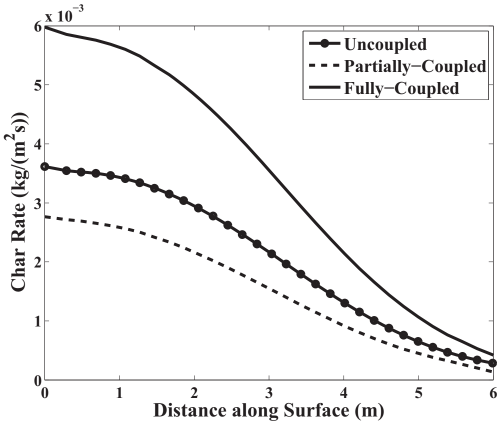

Figure 31: Predicted $\dot{m}_c$ values the 5.26 km/s Mars entry case.

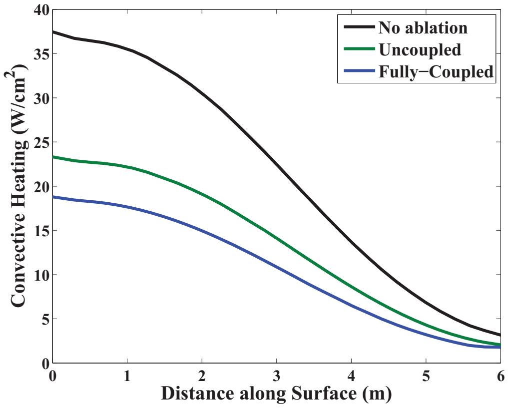

Figure 32: Predicted q_c values the 5.26 km/s Mars entry case.

4.0 COUPLED ANALYSIS OF A COMPLETE MARS RETURN ENTRY TRAJECTORY

The Mars return trajectory considered here is NASA's 50,000 ft/s trajectory, presented in Table 9. This trajectory was studied considerably in the 1960s and 70s as a benchmark Mars return case. The geometry is chosen as a 3.1 m sphere to approximate the Apollo stagnation region. The heat shield is set to 4.5 cm of Pioneer-Venus heritage carbon phenolic. This would approximately double the heat shield mass relative to Apollo's Avcoat heat shield.

The solution procedure for obtaining a fully coupled ablation and radiation solution, with the pyrolysis rate and q_{cond} obtained from a material response code, consists of obtaining a steady state ablation solution for each point in the trajectory. The wall temperatures and char rates obtained from these solutions are then applied as inputs to a material response code, which outputs the pyrolysis rate and q_{cond}. Coupled flowfield solutions are then recomputed with the steady state ablation approximation removed to obtain updated wall temperatures and char rates. This process is repeated until the char and pyrolysis rates are unchanged between iterations.

The peak heating region of the trajectory between t = 7.4 – 110 s, which contains the most significant radiation and ablation coupling, is considered in Section 4.0.1, while the later trajectory points between t = 110 – 500 s are considered in Section 4.0.2. The later portion of the trajectory contains significantly weaker heating, char and pyrolysis rates, but is important for sizing the ablator thickness due to the redistribution of the sharp temperature gradients present through the material at the end of the peak heating trajectory phase. This temperature redistribution through conduction drives the temperature at the ablator–structure interface (bondline temperature), which represents one of the primary design constraints for choosing the ablator thickness. The design limit for the bondline temperature depends on the bonding agent between the ablator and supporting

Table 9: Free-stream conditions for the Mars return trajectory.

time (s)	Velocity (km/s)	density (kg/m^3)	Temperature (K)
7.4	14.74	1.35e-7	221.9
15	14.74	1.43e-6	173.2
22	14.76	1.54e-5	165.6
29	14.76	6.89e-5	198.1
37	14.52	1.83e-4	229.7
45	14.08	3.79e-4	256.6
52	13.54	4.73e-4	265.3
59	12.86	4.73e-4	265.3
67	12.19	4.73e-4	265.3
74	11.65	4.73e-4	265.3
82	11.11	4.73e-4	265.3
89	10.67	4.73e-4	265.3
104	9.77	4.73e-4	265.3
111	9.50	4.73e-4	265.3
119	9.16	4.73e-4	265.3
130	8.75	4.73e-4	265.3
150	8.06	4.73e-4	265.3
200	6.77	4.73e-4	265.3
300	5.09	4.73e-4	265.3
400	3.99	6.08e-4	262.3
450	3.41	9.79e-4	261.1
500	2.68	2.19e-3	260.1

structure, and range between 600 – 800 K. A limit of 600 K is considered in this work.

4.0.1 Analysis of Peak Heating Region of Trajectory

Figure 33 presents the char rate, pyrolysis rate, and wall temperatures obtained from the initial steady state ablation approximation and the final solution coupled with the material response code. The significant differences between the pyrolysis rates seen early in the trajectory are to be expected, since the steady-state ratio of char and pyrolysis rates is fixed by Eq. (30). The difference between the magnitude of the char rate peaks is a result of the steady state approximation of q_{cond} implied in Eq. (29). Because this peak ablation region is sublimation dominated, the char rate is sensitive to the wall temperature, and therefore the energy equation. The radiative and convective heating along the trajectory are presented in Fig. 33 for the steady state and detailed solutions. The relatively good agreement between the steady-state and detailed heating confirms that q_{cond} is responsible for the difference in peak char rates. Note that the details of the stagnation point radiative heating at $t = 45$ s was presented in Section 2.4. The wall temperatures along the trajectory presented in Fig. 35 show the expected result of lower temperatures in the early part of the trajectory for the detailed solution. The larger pyrolysis rates and q_{cond} for the detailed solution are responsible for these lower temperatures.

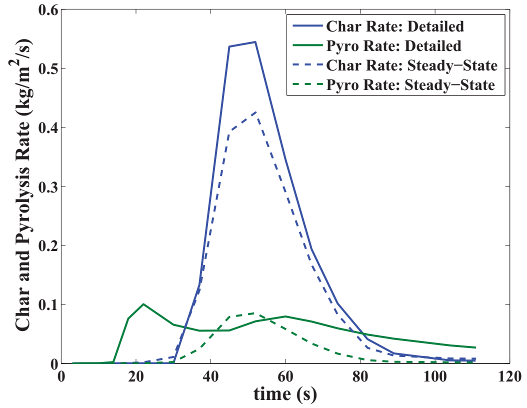

Figure 33: Simulated char and Pyrolysis injection rates at the stagnation point for the Mars return trajectory.

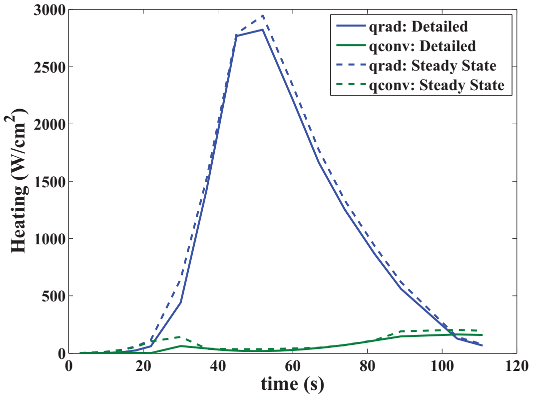

Figure 34: Simulated radiative and convective at the stagnation point for the Mars return trajectory.

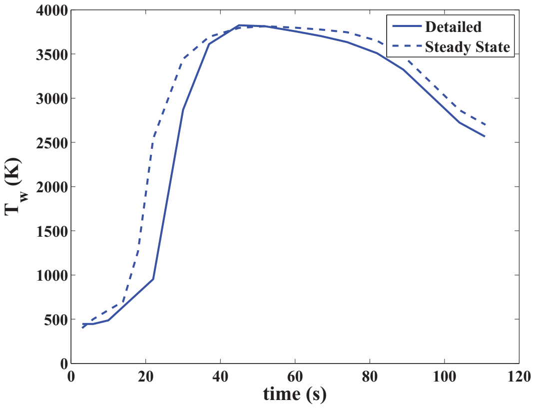

Figure 35: Simulated wall temperatures at the stagnation point for the Mars return trajectory.

The temperature and density profiles through the ablator at the stagnation point, for various trajectory points, are presented in Figs. 36 and 37. Recession is indicated in these figures by the gradual change in the minimum “distance into the heatshield” for each trajectory point. The temperature profiles in Fig. 36 indicate that the ablator has provided successful protection through the peak heating phase of the trajectory, with the temperatures at the back of the heatshield remaining at their ambient values with 1.5 cm of ablator to spare. However, as the temperature gradients seen here are redistributed in the later phase of the trajectory, the entire 4.5 cm of ablator will be required to keep the bondline temperature below 600 K, as shown in the next section. Figure 37 shows the transition from the char at 1179 kg/m^3 through the pyrolysis zone and to the virgin material at 1464 kg/m^3. The significant recession is seen to limit the thickness of the char throughout most of the trajectory.

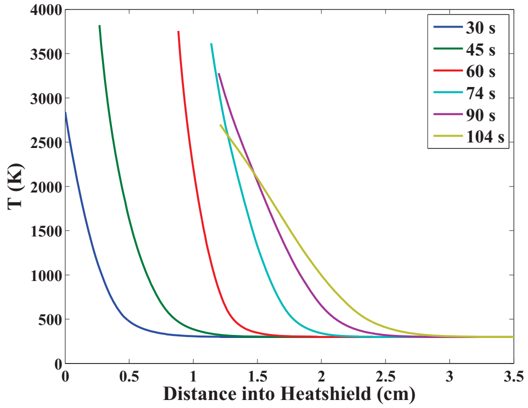

Figure 36: Temperature profiles through the ablator at the stagnation point for the Mars return trajectory.

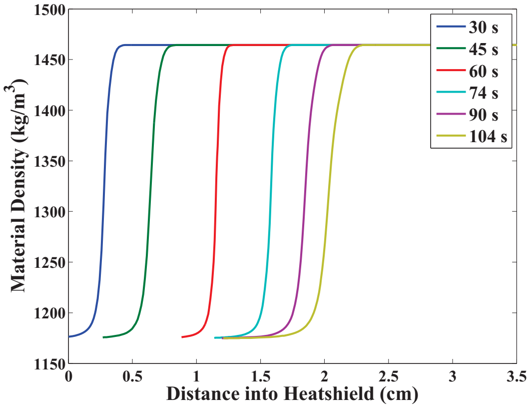

Figure 37: Density profiles through the ablator at the stagnation point for the Mars return trajectory.

Considering the non-stagnation point results, Figures 38 – 42 present the radiative heating, convective heating, char rates, pyrolysis rates, and wall temperatures along the body at various trajectory points. An observation of note from these figures is that the convective heating, which is assumed laminar, is largest downstream of the stagnation point where the ablation rates are lower. However, these peak values are negligible relative to the local radiative heating, except at the late 90 and 104 s trajectory points. Future studies should treat the more realistic turbulent case, which will result in larger convective heating values.

Another important observation from these figures is that the pyrolysis rates are dominant in the far downstream region, where the heating is still relatively high, but the lower pressure reduces the char rates. This is seen more clearly in Fig. 43, which presents the distance of the of the surface (recession) and pyrolysis zone interface at the end of the considered trajectory. It is seen that beyond 3 m the recession is negligible while the pyrolysis zone has proceeded considerably into the surface.

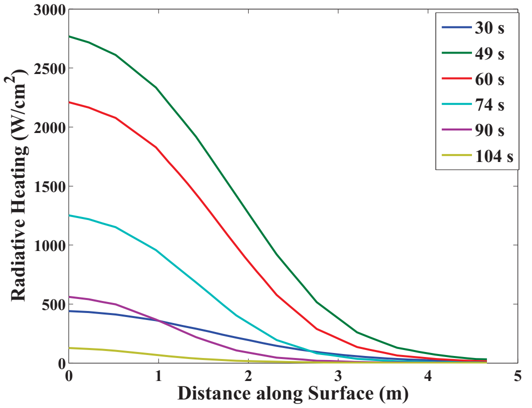

Figure 38: Radiative heating along the body for a range of trajectory points.

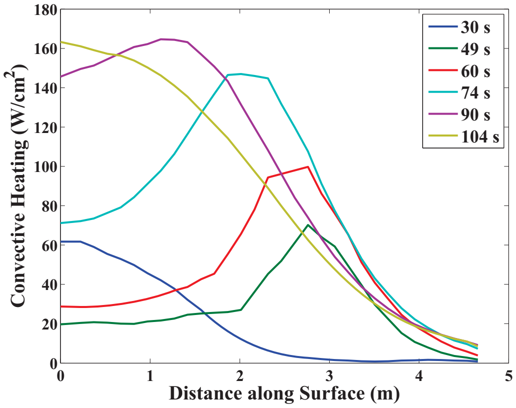

Figure 39: Convective heating along the body for a range of trajectory points.

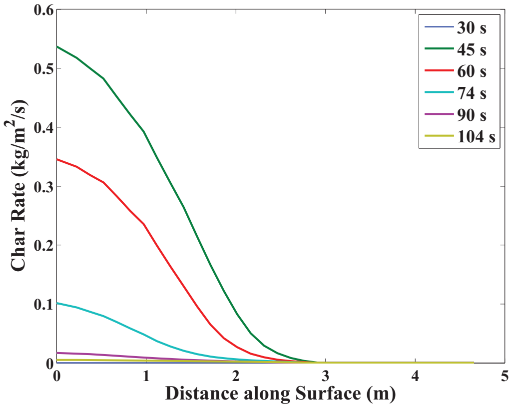

Figure 40: Radiative heating along the body for a range of trajectory points.

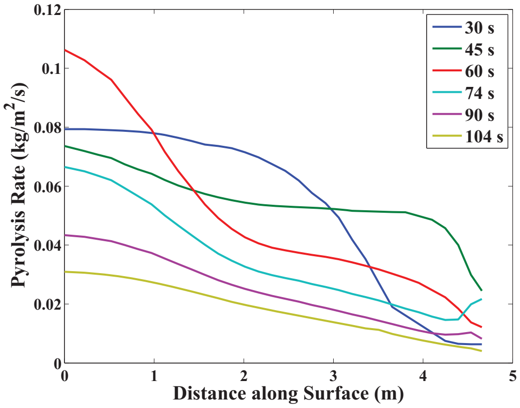

Figure 41: Convective heating along the body for a range of trajectory points.

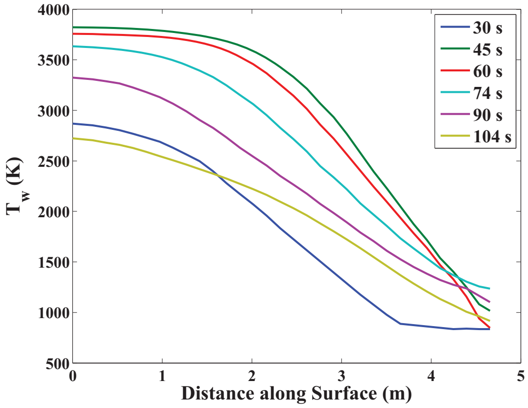

Figure 42: Surface temperature along the body for a range of trajectory points.

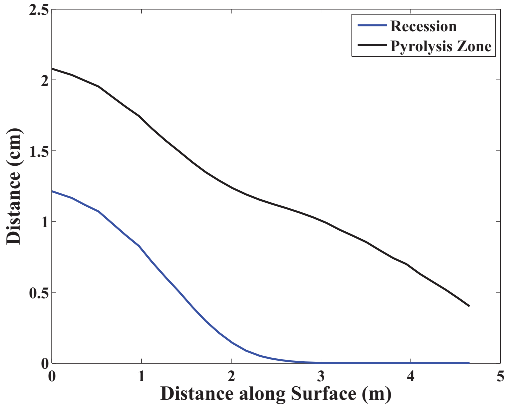

Figure 43: Recession and pyrolysis zone interface, both relative to the original surface location, at t=110 s.

4.0.2 Analysis of Cool Down Region of Trajectory

The char and pyrolysis rates at the stagnation point during the later the part of the trajectory are presented in Fig. 44, while the corresponding heating rates and wall temperatures are presented in Figs. 45 and 46. The char rates are seen to be two orders of magnitude lower than the peak char rate, which is a result of this trajectory region being dominated by diffusion limited oxidation. Figure 45 shows that the radiative heating is negligible in this region.

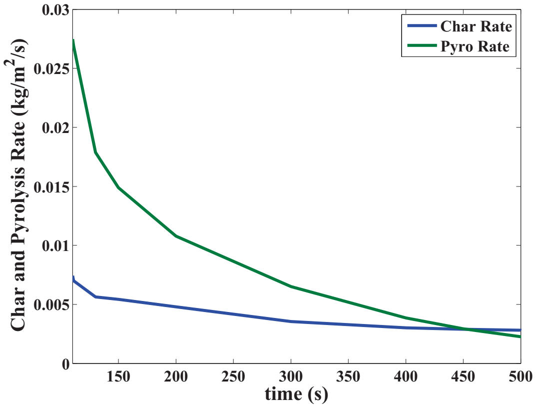

Figure 44: Simulated char and Pyrolysis injection rates at the stagnation point during the later trajectory phase.

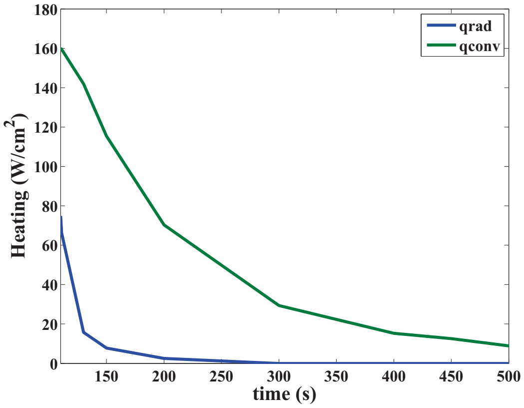

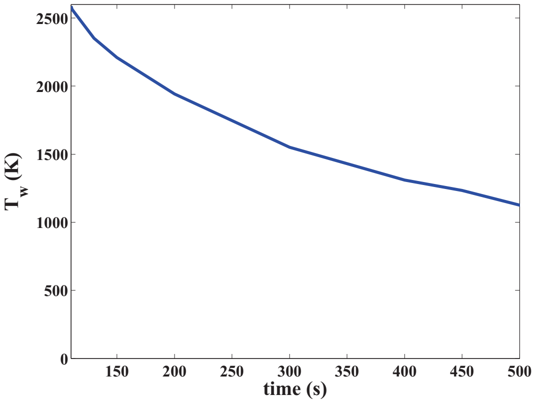

Figure 45: Simulated radiative and convective at the stagnation point during the later trajectory phase.

Figure 46: Simulated wall temperatures at the stagnation point during the later trajectory phase.

The temperature and density distributions through the ablator during the later trajectory points are presented in Figs. 47 and 48. The t = 800 s trajectory point represents the final cool down phase of the trajectory, with a wall temperature specified at 800 K and a char rate set to zero. Figure 47 shows that the bondline temperature remains below 600 K throughout this later phase of the trajectory, while Fig. 48 shows that roughly 0.5 cm of virgin material remains at the end of the trajectory. A comparison of the recession and pyrolysis zone interface at t = 110 s and 800 s is presented in Fig. 49. Although the heating is mild during the later phase, the long time duration is seen to provide significant pyrolysis.

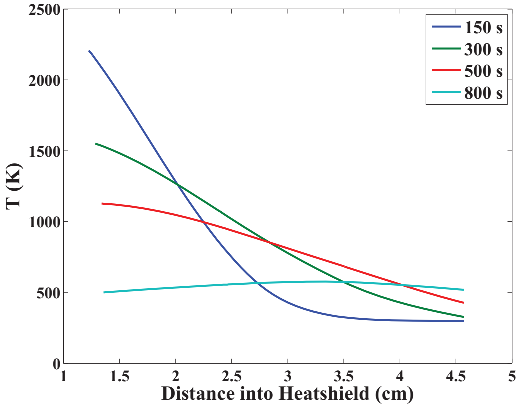

Figure 47: Temperature profiles through the ablator at the stagnation point during the later trajectory phase.

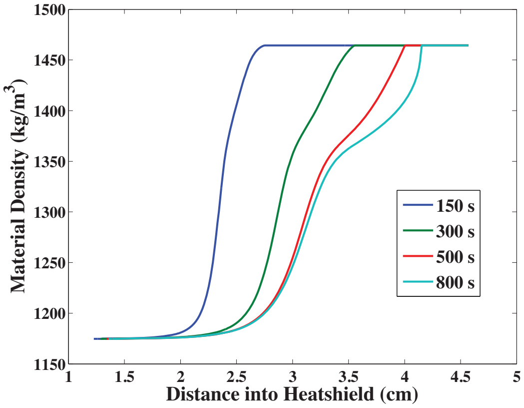

Figure 48: Density profiles through the ablator at the stagnation point during the later trajectory phase.

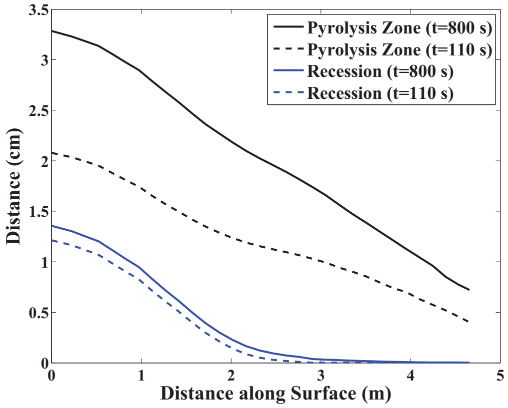

Figure 49: Comparison of recession and pyrolysis zone interfaces, both relative to the original surface location, at t=110 s and 800 s.

4.0.3 Impact of Radiative Heating Uncertainty on Ablator Thickness

The parametric uncertainty of the radiative heating was determined in Section 2.2.2, based on the study of Johnston et al. [23], to be near ±50% for a range of velocities. Applying this uncertainty value as a margin, and recomputing the char rates, surface temperatures, and material response results in a recession of 2.6 cm and pyrolysis zone interface of 4.1 cm. An ablator thickness of 6.2 cm is required to maintain a bondline temperature below 600 K. This nearly 50% increase in the ablator thickness resulting from a 50% increase in the radiative heating indicates the importance of reducing the radiative heating uncertainty at Mars return conditions. Furthermore, this sensitivity requires that ablation and radiation coupling are treated with the highest level of modeling fidelity possible.

REFERENCES

[1] Mazaheri, A., Gnoffo, P. A., Johnston, C. O., and Kleb, B., “LAURA Users Manual,” NASA TM 2010-216836, 2010.

[2] Mcbride, B. J., Zehe, M. J., and Gordon, S., "NASA Glenn Coefficients for Calculating Coefficients for Calculating Thermodynamic Properties of Individual Species," NASA TP 2002–211556, 2002.

[3] Wright, M. J., Bose, D., Palmer, G., and Levin, E., "Recommended Collision Integrals for Transport Property Computations 1: Air Species," *AIAA Journal*, Vol. 43, No. 12, 2005, pp. 2558–2564.

[4] Wright, M. J., Hwang, H., and Schwenke, D. W., "Recommended Collision Integrals for Transport Property Computations Part 2: Mars and Venus Entries," *AIAA Journal*, Vol. 45, No. 1, 2007, pp. 281–288.

[5] Svhehla, R. A., "Estimated Viscosities and Thermal Conductivities of Gases at High Temperatures," NASA TR R 142, 1962.

[6] Park, C., Jaffe, R. L., and Partridge, H., "Chemical-Kinetic Parameters of Hyperbolic Earth Entry," *Journal of Thermophysics and Heat Transfer*, Vol. 15, No. 1, 2001, pp. 76–90.

[7] Johnston, C. O., Gnoffo, P. A., and Mazaheri, A., "A Study of Ablation-Flowfield Coupling Relevant to the Orion Heatshield," AIAA Paper 2009–4318, 2009.

[8] Cebeci, T., "Variation of the Van Driest Damping Parameter with Mass Transfer," *AIAA Journal*, Vol. 11, No. 2, 1973, pp. 237–238.

[9] Cheatwood, F. M. and Thompson, R. A., "The Addition of Algebraic Turbulence Modeling to Program LAURA," NASA TM 107758, 1993.

[10] Babou, Y., Riviere, P., Perrin, M.-Y., and Soufiani, A., "Spectroscopic Data for the Prediction of Radiative Transfer in CO_2-N_2 Plasmas," *Journal of Quantitative Spectroscopy and Radiative Transfer*, Vol. 110, 2009, pp. 89–108.

[11] da Silva, M. L. and Dudeck, M., "Arrays of Radiative Transition Probabilities for CO_2-N_2 Plasmas," *Journal of Quantitative Spectroscopy and Radiative Transfer*, Vol. 102, 2006, pp. 348–386.

[12] Kokkin, D. L., Bacskay, G. B., and Schmidt, T. W., "Oscillator Strengths and Radiative Lifetimes for C_2: Swan, Ballik-Ramsay, Phillips, and $d^3\Pi_g$-$c^3\Sigma_u$," *Journal of Chemical Physics*, Vol. 126, No. 084302, 2007.

[13] Schmidt, T. W. and Bacskayt, G. B., "Oscillator Strengths of the Mulliken, Swan, Ballik-Ramsay, Phillips, and $d^3\Pi_g$-$c^3\Sigma_u$ Systems of C_2 Calculated by MRCI Methods Utilizing a Biorthogonal Transformation of CASSCF Orbitals," *Journal of Chemical Physics*, Vol. 127, No. 234310, 2007.

[14] Cooper, D. M. and Jones, J. J., "An Experimental Determination of the Cross Section of the Swings Band System of C_3," *Journal of Quantitative Spectroscopy and Radiative Transfer*, Vol. 22, 1979, pp. 201–208.

[15] Prakash, S. G. and Park, C., "Shock Tube Spectroscopy of C_3+C_2H Mixture in the 140-700 nm Range," AIAA Paper 1979–0094, 1979.

[16] Shinn, J. L., "Optical Absorption of Carbon and Hydrocarbon Species from Shock Heated Acetylene and Methane in the 135-220 nm Wavelength Range," AIAA Paper 1981–1189, 1981.

[17] Allison, A. C. and Dalgarno, A., "Band Oscillator Strengths and Transitions Probabilities for the Lyman and Werner Systems of H_2, HD, and D_2," *Atomic Data*, Vol. 1, No. 3, 1970, pp. 289–304.

[18] Fabian, W. and Lewis, B. R., "Experimentally Determined Oscillator Strengths for Molecular Hydrogen-I. The Lyman and Werner Bands Above 900 A," *Journal of Quantitative Spectroscopy and Radiative Transfer*, Vol. 14, 1974, pp. 523–535.

[19] Lewis, B. R., "Experimentally Determined Oscillator Strengths for Molecular Hydrogen-II. The Lyman and Werner Bands Below 900 A." *Journal of Quantitative Spectroscopy and Radiative Transfer*, Vol. 14, 1974, pp. 537–546.

[20] Brewer, L. and Engelke, J. L., "Spectrum of C_3," *Journal of Chemical Physics*, Vol. 36, No. 4, 1962, pp. 992–998.

[21] Moss, J. N., Jones, J. J., and Simmonds, A. L., "Radiative Flux Penetration Through a Blown Shock Layer," AIAA Paper 1978–908, 1978.

[22] Arnold, J. O., Cooper, D. M., Park, C., and Prakash, S. G., "Line-by-Line Transport Calculations for Jupiter Entry Probes," AIAA Paper 1979–1082, 1979.

[23] Johnston, C., Mazaheri, A., Gnoffo, P., Sutton, K., Brandis, A., Prabhu, D., and Bose, D., "Assessment of Radiative Heating Uncertainty for Hyperbolic Earth Entry," AIAA Paper 2011–3145, 2011.

[24] Johnston, C. O., Brandis, A. M., and Sutton, K., "Shock Layer Radiation Modeling and Uncertainty for Mars Entry," AIAA Paper 2012–2866, 2012.

[25] Stanley, S. A. and Carlson, L. A., "Effects of Shock Wave Precursor Ahead of Hypersonic Entry Vehicles," *Journal of Spacecraft & Rockets*, Vol. 29, No. 2, 1992, pp. 190–197.

[26] Romanov, G. S., Stankevich, Y. A., Stanchits, L. K., and Stepanov, K. L., "Thermodynamic and Optical Properties of Gases in a Wide Range of Parameters," *International Journal of Heat and Mass Transfer*, Vol. 38, No. 3, 1995, pp. 545–556.

[27] Johnston, C. O., Hollis, B. R., and Sutton, K., "Spectrum Modeling for Air Shock-Layer Radiation at Lunar-Return Conditions," *Journal of Spacecraft & Rockets*, Vol. 45, Sep.-Oct. 2008, pp. 865–878.

[28] Zeldovich, Y. B. and Raizer, Y. P., *Physics of Shock Waves and High Temperature Hydrodynamic Phenomena*, Academic Press, New York and London, 1967.

[29] Yoshikawa, K. K., "Analysis of Radiative Heat Transfer for Large Objects at Meteoric Speeds," NASA TN 4051, 1967.

[30] Lasher, L. E. and Wilson, K. H., "Effect of Shock Precursor Heating on Radiative Flux to Blunt Bodies," NASA CR 1265, 1969.

[31] Vertushkin, V. K. and Romishevskii, E. A., "Influence of the Precursor Effect on Hypersonic Blunt Body Flow," *Fluid Dynamics*, , No. 6, 1970, pp. 933–939.

[32] Zinn, J. and Anderson, R. C., "Structure and Luminosity of Strong Shock Waves in Air," *The Physics of Fluids*, Vol. 16, No. 10, 1973, pp. 1639–1644.

[33] Nemtchinov, I. V., Popova, O. P., Shuvalov, V. V., and Svetsov, V. V., "Radiation Emitted During the Flight of Asteroids and Comets through the Atmosphere," *Planetary and Space Sciences*, Vol. 42, No. 6, 1994, pp. 491–506.

[34] Golub, A. P., Kosarev, I. B., Nemchinov, I. V., and Shuvalov, V. V., "Emission and Ablation of a Large Meteoroid in the Course of Its Motion Through the Earth's Atmosphere," *Solar System Research*, Vol. 30, No. 3, 1996, pp. 213–228.

[35] Gnoffo, P. A., Johnston, C. O., and Thompson, R. A., "Implementation of Radiation, Ablation, and Free-Energy Minimization in Hypersonic Simulations," *Journal of Spacecraft & Rockets*, Vol. 47, No. 2, 2010, pp. 481–491.

[36] Bauman, P. T., Stogner, R., Carey, G. F., Schulz, K. W., Upadhyay, R., and Maurente, A., "Loose-Coupling Algorithm for Simulating Hypersonic Flows with Radiation and Abaltion," *Journal of Spacecraft & Rockets*, Vol. 48, No. 1, 2011, pp. 72–80.

[37] Cunto, W., Mendoza, C., Ochsenbein, F., and Zeippen, C., "TOPbase at the CDS," *Astronomy and Astrophysics*, Vol. 275, Aug. 1993, pp. L5–L8, see also vizier.u-strasbg.fr/topbase/topbase.html.

[38] Thompson, R. A. and Gnoffo, P. A., "Implementation of a Blowing Boundary Condition in the LAURA Code," AIAA Paper 2008–1243, 2008.

[39] Martinelli, S., Ruffin, S., McDaniel, R., Brown, J., Wright, M., and Hash, D., "Validation Process for Blowing and Transpiration Cooling in DPLR," AIAA Paper 2007–4255, 2007.

[40] Lees, L., "Convective Heat Transfer with Mass Addition and Chemical Reactions," Combustion and propulsion third agard colloquium, March 1958.

[41] Bianchi, D., Nasuti, F., Martelli, E., and Onofri, M., "A Numerical Approach for High-Temperature Flows over Ablating Surfaces," AIAA Paper 2007–4537, June 2007.

[42] Bartlett, E. P., Abbett, M. J., Nicolet, W. E., and Moyer, C. B., "Improved Heat-Shield Design Procedures for Manned Entry Systems," NASA CR 108689, 1970.